Geomorphology 488 (2025) 109961

Contents lists available at ScienceDirect

Geomorphology

journal homepage: www.journals.elsevier.com/geomorphology

Very fast canyon formation and evolution along active volcanic flanks: A case from Stromboli Island

Daniele Casalbore [a,b], Federico Di Traglia [c,d,e], Massimiliano Favalli [f], Alessandro Fornaciai [f,*], Claudia Romagnoli [b,g], Riccardo Civico [h], Tullio Ricci [h], Paolo Berardino [d], Lorenzo Borselli [i,j], Pierfrancesco Calabria [c], Sonia Calvari [k], Tommaso Carlà [e], Nicola Casagli [e,l], Francesco Casu [d], Francesco Latino Chiocci [a,b], Walter De Cesare [c], Claudio De Luca [d], Matteo Del Soldato [e], Antonietta M. Esposito [c], Carmen Esposito [d], Flora Giudicepietro [c,d], Teresa Gracchi [e,l], Riccardo Lanari [d], Giovanni Macedonio [c,d], Fernando Monterroso [d], Antonio Natale [d], Teresa Nolesini [m], Stefano Perna [d,n], Denise Petronelli [a], Guglielmo Rossi [m], Carlo Tacconi Stefanelli [e]

[a] *Dipartimento di Scienze della Terra, Università degli Studi di Roma "La Sapienza", Piazzale Aldo Moro 5, 00185 Rome, Italy*
[b] *Consiglio Nazionale delle Ricerche, Istituto di Geologia Ambientale e Geoingegneria (CNR-IGAG), UO Sapienza, Piazzale Aldo Moro, 7, 00185 Rome, Italy*
[c] *Istituto Nazionale di Geofisica e Vulcanologia, Osservatorio Vesuviano, Via Diocleziano 328, 80124 Naples, Italy*
[d] *Consiglio Nazionale delle Ricerche, Istituto per il Rilevamento Elettromagnetico dell'Ambiente (CNR-IREA), Via Diocleziano 328, 80124 Naples, Italy*
[e] *Dipartimento di Scienze della Terra, Università degli Studi di Firenze, Via La Pira 4, 50121 Florence, Italy*
[f] *Istituto Nazionale di Geofisica e Vulcanologia, Sezione di Pisa, Via Cesare Battisti, 53, 56125 Pisa, Italy*
[g] *Dipartimento Scienze Biologiche, Geologiche e Ambientali, Università degli Studi di Bologna, P.zza Porta S. Donato 1, 40126 Bologna, Italy*
[h] *Istituto Nazionale di Geofisica e Vulcanologia, Sezione Roma 1, Via di Vigna Murata 605, 00143 Rome, Italy*
[i] *Facultad de Ingenieria, Instituto de Geologia, Universidad Autonoma de San Luis Potosì (UASLP), Av. Dr. Manuel Nava 5, 78290 San Luis Potosí, Mexico*
[j] *Istituto Di Ricerca Per La Protezione Idrogeologica (CNR-IRPI), Consiglio Nazionale Delle Ricerche, Via Madonna Alta 126, 06128 Perugia, Italy*
[k] *Istituto Nazionale di Geofisica e Vulcanologia, Osservatorio Etneo, Piazza Roma 2, 95125 Catania, Italy*
[l] *National Institute of Oceanography and Applied Geophysics - OGS, Borgo Grotta Gigante 42/C, 34010 Sgonico, Italy*
[m] *Centro Per La Protezione Civile, Università degli Studi di Firenze, Piazza San Marco 4, 50121 Florence, Italy*
[n] *Dipartimento di Ingegneria, Università degli Studi di Napoli Parthenope, Naples, Italy*

ARTICLE INFO

Keywords:
Volcano geomorphology
Submarine erosion
Canyon
Slope instability
Pyroclastic density currents
stromboli volcano

ABSTRACT

Active insular volcanoes are generally characterized by their rapid morphological evolution, as a close interplay exists between eruptive activity and erosive-depositional processes in such volcanoes. The Sciara del Fuoco depression, a sector collapse scar on the NW flank of the Stromboli volcano (Italy), is considered a natural laboratory for studying the response of a volcanic slope to such a dynamic evolution. In this study, we report the very fast morphological evolution that affected the subaerial and submarine Sciara del Fuoco slope from May 2022 to May 2023, a period of time marked by the occurrence of two crater rim failures, pyroclastic density currents and multiple lava flows. The analysis of repeated topo-bathymetric surveys demonstrates that a narrow (100 m wide at maximum) and steep-sided canyon, tens of meters deep, formed in the central part of the Sciara del Fuoco. The canyon was mainly related to the erosive activity of the pyroclastic density currents, which led to the remobilization of (at least) 3.7×10^6 m^3 volcanic material, mainly in the subaerial slope. The canyon was initially formed by retrogressive erosion upslope, starting from an initial submarine/coastal landslide. It then evolved through a progressive widening of its flanks through small-scale landslides. The study shows that landslide location, as well as the final canyon shape, were strongly controlled by the lithological limits of previous lava flows, highlighting the importance of inherited morpho-stratigraphy and lateral heterogeneities in slope stability. Since its formation, the canyon has acted as a main conduit for lava flows and volcaniclastic materials supplied on their way to the sea. About 1×10^6 m^3 of material filled the subaerial canyon floor through time, and another 1×10^6 m^3 of slope accretion was estimated for the submarine part of the Sciara del Fuoco,

* Corresponding author.
E-mail address: alessandro.fornaciai@ingv.it (A. Fornaciai).

https://doi.org/10.1016/j.geomorph.2025.109961
Received 22 January 2025; Received in revised form 27 May 2025; Accepted 4 August 2025
Available online 7 August 2025

down to 400 m below sea level. Comparing the volumes associated with slope erosion and accretion, it is evident that a large part of the remobilized material bypassed the Sciara del Fuoco shallow-water sector and was emplaced at greater depths. This study highlights the relevance of an integrated system for monitoring the submarine and subaerial morphological evolution of insular volcanic flanks, contributing to an improved geohazard assessment during eruptive crises.

List of the acronyms used in this paper

asl	above sea level
bsl	below sea level
DEM	Digital Elevation Model
DGPS	Differential Global Position System
DoD	DEM of Difference
ELO	Early Lava Overflows
GCP	Ground Control Point
GPS	Global Position System
INGV-OE	Istituto Nazionale di Geofisica e Vulcanologia - Osservatorio Etneo
LiDAR	Light Detection And Ranging
NEC	North-East Crater
PDCs	Pyroclastic Density Currents
RMS	root mean square
ROV	Remotely Operated Vehicle
RTK	Real Time Kinematic positioning
SCT	Stromboli thermal camera located at Labronzo
SCV	Stromboli visible camera located at Labronzo
SdF	Sciara del Fuoco
SQV	Stromboli visible camera located at 400 m asl
SP InSAR	Single-Pass Interferometric Synthetic Aperture Radar
SPCT	Stromboli thermal camera located at Punta dei Corvi
SPT	Stromboli thermal camera located at Il Pizzo
SWC-CC	SW-Central Crater
UAS	Unoccupied Aircraft System
UTC	Coordinated Universal Time

1. Introduction

The steep flanks of active stratovolcanoes are prone to rapid geomorphological changes due to their frequent eruptive activity (Thouret, 1999). One of the best examples is the NW flank of Stromboli volcano, where the present-day slope of a partially filled collapse scar, the Sciara del Fuoco (SdF, hereafter), shows significant geomorphological changes in short time periods (from days to months). These changes are associated with the accumulation of volcaniclastic deposits, lava flows, and their subsequent reworking by mass flows and exogenous phenomena, such as sea waves (Kokelaar and Romagnoli, 1995; Casalbore et al., 2010; Di Traglia et al., 2018a, 2020; Tioukov et al., 2022). The SdF itself shows persistent small-scale instability phenomena such as rockfalls and debris slides with a volume of less than 10^4 m^3 (Di Traglia et al., 2018b). Occasionally, larger landslides of tens to hundreds of millions of cubic metres of rock and volcaniclastic debris occur in its interior (Chiocci et al., 2008a; Rosi et al., 2019). The gradual and commonly fast morphologic readjustment of the SdF slope typically reduces the preservation potential of these features, which tend to be obliterated in a relatively short time (Chiocci et al., 2008b).

This work analyses the morphological response of SdF to a period of increased eruptive activity at the Stromboli summit craters between May 2022 and May 2023, with the occurrence of two crater rim collapses, several pyroclastic density currents (PDCs, hereafter) and lava overflows from the crater rim (Giudicepietro et al., 2023; Di Traglia et al., 2024). During this period, a narrow and steep-sided canyon, tens of metres deep, rapidly (only one week) formed in the subaerial part of SdF. The development of a similar erosive feature is, to our knowledge, undocumented in the historical evolution of the subaerial SdF reconstructed since 1868 (e.g., Marsella et al., 2012) and through the setup of an integrated monitoring system of the SdF slope after the 2002 tsunamigenic landslide (Bonaccorso et al., 2003; Calvari et al., 2005; Esposito et al., 2012).

Through the analysis of multi-temporal topographic and bathymetric surveys, combined with volcanological observations from the fixed monitoring camera network operated by Osservatorio Etneo (Istituto Nazionale di Geofisica e Vulcanologia, INGV-OE) and videos recorded from Unoccupied Aircraft System (UAS), this work is aimed at addressing the following research questions:

1) Which were the main factors that controlled the formation of the subaerial canyon on SdF in a very short time period and its later evolution?
2) How did the canyon formation influence the morphological evolution of the submarine slope?;
3) Which are the main implications in terms of geohazard assessment?

By answering these questions, this study provides new insights on the combined morphological response of insular volcanic flanks to eruptive dynamics, with reference to small/medium-scale instability of volcaniclastic deposits and deposit-derived PDCs, a topic often overlooked in literature for large-scale processes. Moreover, the unique possibility to monitor the canyon formation in such rapid times is potentially of large interest for geomorphological studies elsewhere as well as for the proper management of future eruptive crises at Stromboli.

2. Stromboli volcano and its recent activity

Stromboli is a large insular volcano in the Tyrrhenian Sea (see Fig. 1a, b), known for its persistent and mild explosive “Strombolian” activity (Mercalli, 1883). Throughout its history, Stromboli has recorded distinct phases of activity, which were often accompanied by bilateral flank instability events on its NW and SE slopes (Romagnoli et al., 2009a, 2009b). The NW flank was affected by a series of significant lateral collapses in the last 13 ka (Francalanci et al., 2013), the last of them occurred during the Middle Ages and accompanied by tsunamigenic events (Rosi et al., 2019; Pistolesi et al., 2020). The NW flank of the volcano is morphologically dominated by the 2 km-wide SdF collapse scar, where a summit crater terrace is present with three emission craters and a variable number of active vents (Civico et al., 2021) (Fig. 1c). The SdF scar extends down to 700 m below sea level (bsl, hereafter) and is very steep, with average slope gradients of 35° for its subaerial part, 30° in the first 200–300 m bsl and 20° at greater depths (Romagnoli et al., 2009b). The SdF experienced sporadic effusive eruptions, with volumes ranging from a few tens to several millions of cubic metres (Marsella et al., 2012; Di Traglia et al., 2020; Casalbore et al., 2022; Calvari and Nunnari, 2023). Occasionally, prolonged flank eruptions from eruptive vents on the SdF slope led to the formation of lava deltas, followed by their gradual erosion (e.g., Bosman et al., 2014; Di Traglia et al., 2018c).

The accumulation of volcaniclastic and lava flows within the SdF

collapse scar alternates with erosion and mass flow events (Kokelaar and Romagnoli, 1995). The French geologist Déodat Guy Silvain Tancrède Gratet de Dolomieu, during his travel to the Aeolian Islands from 12 to 21 July 1781, reported that "*for a long time this volcano has not erupted any real lavas, but only sand and porous black and reddish lavas*" (de Dolomieu, 1783). Planar and rotational slides developing into rock/debris avalanches, each with an estimated volume of tens of millions of cubic metres and tsunamigenic, have been reported in the last century and directly observed on 30 December 2002 (e.g., Maramai et al., 2005). The latter event was triggered by magma intrusion into the SdF, leading to the onset of the 2002–2003 flank eruption (Bonaccorso et al., 2003; Calvari et al., 2005; Verrucci et al., 2019; Di Traglia et al., 2023a). The landslide involved a complex mass movement with a slope failure of about 20 million cubic metres in the subaerial and submarine SdF slopes. These types of landslides can generate tsunamis with significant impact on Stromboli and the surrounding coasts (e.g., Tinti et al., 2005; Fornaciai et al., 2019).

After the 30 December 2002 landslide, Stromboli experienced long periods of material accumulation in the SdF, caused by flank eruptions (2002–03, 2007, 2014, 2019; Calvari et al., 2005, 2010; Giudicepietro et al., 2020; Di Traglia et al., 2022). In addition, there were phases of more intense eruptive activity, characterized by frequent explosions, lava fountains and lava overflows from the crater terrace and collapses of the crater rim. These rapidly led to significant slope accumulation and erosion over the SdF, mostly extending to a depth of 300 m (Fig. 1c; Casalbore et al., 2020; Di Traglia et al., 2018a, 2021). Some of these events were able to generate significant seafloor erosion/slope instability (Di Traglia et al., 2022, 2023b; Casalbore et al., 2022) and small tsunami waves (Ripepe and Lacanna, 2024). Conversely, during periods of reduced explosion frequency and intensity, the dominant processes observed were subaerial erosion and marine-driven reworking (Falsaperla et al., 2008; Di Traglia et al., 2018b, 2020; Casalbore et al., 2020).

2.1. Summary of eruptive activity between May 2022 and March 2023

During this period, the persistent Strombolian explosive activity of Stromboli volcano was accompanied by some major explosions and lava overflows from the summit craters, as summarised in Fig. 2 and Table 1ESM (for more details, see Di Traglia et al., 2024). An event that significantly altered the SdF morphology occurred between 9 and 15 October 2022 and resulted in the formation of a canyon in the central part of the SdF.

The sequence began with the destabilisation of the crater rim, with a minimum mobilized volume of ~6×10^3 m^3, leading to the formation of PDCs at 07:22 of October 9, followed by lava overflow from the collapsed region (Giudicepietro et al., 2023; Di Traglia et al., 2024). The PDC rapidly reached the shoreline with a velocity of about 62 m/s. Other two PDCs reached the coast and beyond at 7:34 and again at 7:43. The latter, according to SPCT observations, did not originate from the crater

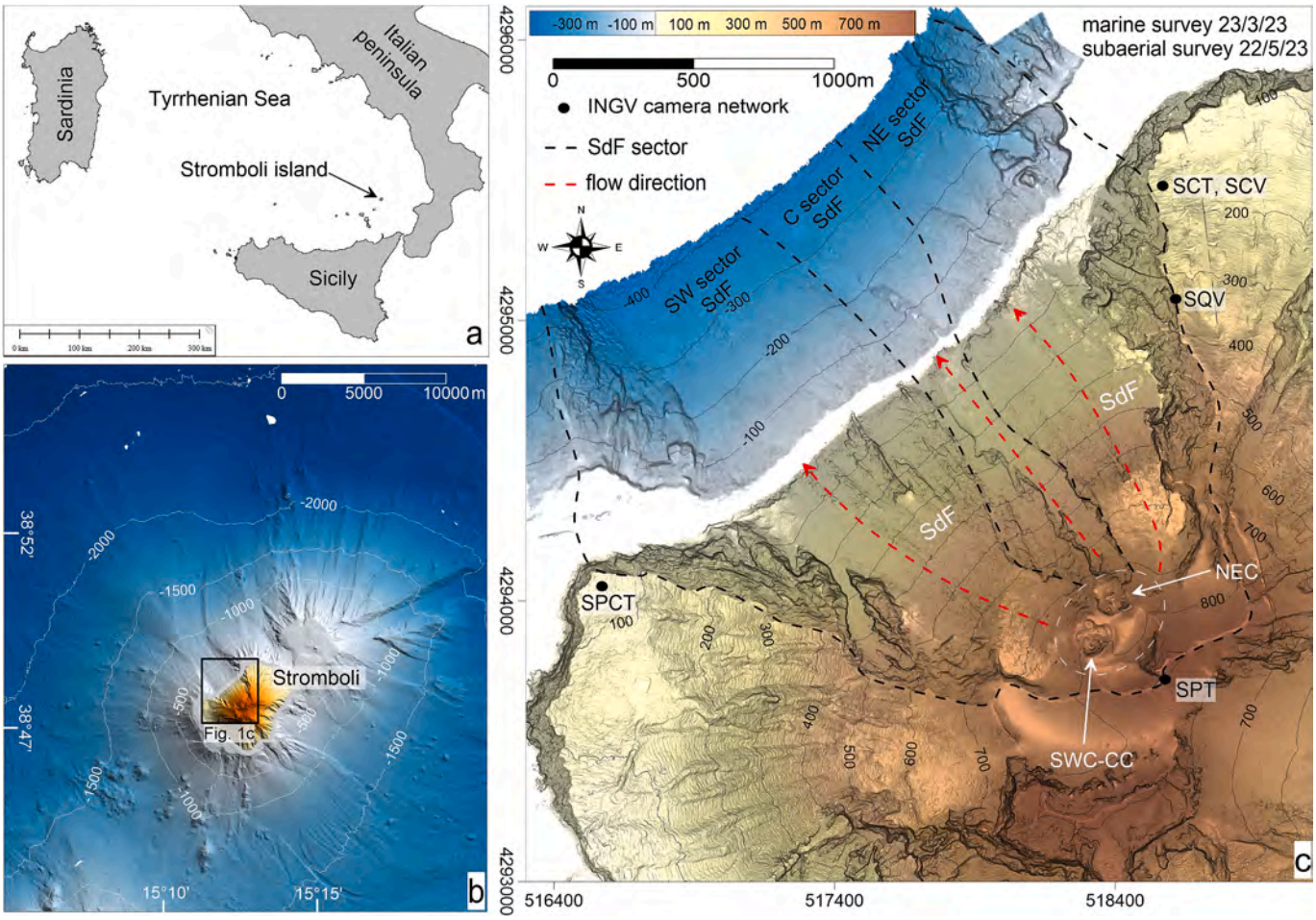

Fig. 1. a) Location of Stromboli Island within the southern Tyrrhenian Sea. b) Shaded relief map and isobaths of the Stromboli edifice, with location of the study area (black box). c) Shaded relief model, based on high-resolution DEMs, revealing the morphology of the island and the submarine part (down to about 400 m depth) of SdF. Dashed black lines show the lateral limits of SdF and its subdivision in south-western, central and north-eastern SdF sectors. Trajectories of distinct flow zones, as identified by Di Traglia et al. (2018b), are highlighted with red arrows. The position of the summit crater terrace (dashed white lines), the main eruptive vents and the fixed monitoring cameras (SPCT, SPT, SCT, SCV and SQV) are also marked. SWC-CC, NEC: South-West-Central and North-East craters.

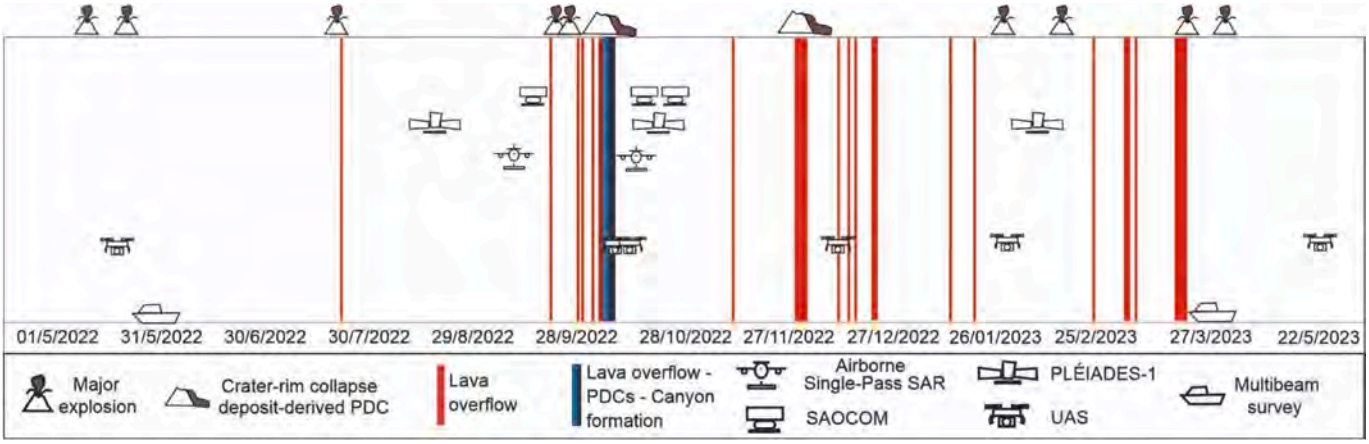

Fig. 2. Chronology of data acquisition between May 2022 and May 2023 and main eruptive events in the same period.

but appeared to come from a source located about 400 m below, probably triggered by blocks detached from the advancing lava front. UAS observations provided important insights both on the initiation of the failure of volcaniclastic deposit along SdF, and on the later morphological changes caused by the erosion of the SdF slope.

In particular, the observations made on 9 October 2022 at 07:59 showed muddy (turbid) water in the marine area facing SdF (Fig. 3a), probably due to the initial flow of the PDCs into the sea. The same survey showed that the coastal morphology changed significantly during this period, with lava accumulation in the central sector of SdF (mainly along

Fig. 3. Photographs taken during the UAS surveys on 9 October 2022 (courtesy of Stefano Cannavò) provide valuable insights on the occurring phenomena. In photo a), taken at 07:59, an area of muddy (turbid) water is outlined, likely corresponding to the region where the initial PDC reached the water surface, resulting in subsequent mixing of material with sea water. In b), taken during the same survey as a), a landslide scar in the coastal area is outlined, highlighting the occurrence of instability phenomena from the early moments of the effusive phase. Photos taken at c) 08:11 and d) 16:24 show that the PDCs, involving volcaniclastic material collected within SdF, were associated with the deposition along the slope and down to its base and had their source in the landslide scar shown in b).

its SW part, early lava overflows in Fig. 3b) and the appearance of a landslide scar along the coastline, close to the point where the first PDC and lava overflows entered the sea (Fig. 3b). Images taken on the same day showed that the PDCs originating from the volcaniclastic material within the SdF were initiated upslope of the landslide scar (Fig. 3c, d). This process continued over the following days, with the initiation point of the PDCs gradually rising to higher elevations and finally ceasing on 17 October 2022. Following this period, volcanic activity remained at medium levels, punctuated by powerful explosions and ejection of bombs and spatter as well as by small lava overflows, as occurred on 16 November 2022 (Giudicepietro et al., 2023; Calvari and Nunnari, 2023). Another period of repeated crater rim collapses coupled with PDCs and lava overflows from the crater rim occurred between 4 and 8 December 2022 (Fig. 2 and Table 1ESM). A first major failure from the crater rim occurred at 14:28 on 4 December 2022, with an estimated volume of $\sim 8.9 \times 10^4$ m^3 (Di Traglia et al., 2024) and caused a PDC spreading along the SdF slope. This event was followed by at least 3–4 additional pulses of PDCs occurring between 14:31 and 14:33. These repeated failures deeply eroded the flank of the northeast crater (NEC, hereafter), likely enhanced by two lava channels spreading from the breached NEC along SdF. At 15:18, a new major failure took place from the crater rim, causing a thick and hot ash cloud. Several failures occurred from this crater rim and from several points along the SdF slope, feeding PDCs and a thick ash cloud for about 2 h, then gradually declining. The failures left half of the NE cone, with the conduit exposed to feed a lava flow spreading along the SdF slope and reaching the sea, as witnessed by a white steam cloud spread towards the craters and above the PDC. The effusive activity continued until 8 December 2022, mostly obscured to the monitoring cameras field of view because of spreading within the saddle left by the failure along the SdF. After that, other main lava overflows occurred on 16, 19, 21, 26–27 December 2022; 2, 4, 17 and 24 January 2023; 27 February 2023; 8, 9, 11 and 23 March 2023 (Fig. 2 and Table 1ESM). Two major explosions occurred on 25 March and 7 April 2023.

3. Material and methods

3.1. Volcanological observations and webcam images

The continuous monitoring of Stromboli's eruptive activity and the quantification of explosive events observed at the summit vents were conducted through a visual analysis of images captured by the fixed monitoring camera network operated by the INGV-OE. This network includes three thermal cameras situated at Il Pizzo Sopra La Fossa (SPT), Punta dei Corvi (SPCT), and Semaforo Labronzo (SCT), as well as one visible camera positioned at Semaforo Labronzo (SCV) and another visible camera (SQV) located at 400 m asl along the eastern rim of the SdF (Fig. 1c, for more details on the main characteristics of the cameras refer to Di Traglia et al., 2024).

3.2. Topographic and bathymetric surveys

To investigate the geomorphological evolution and dynamics of the SdF, we conducted multi-temporal topographic and bathymetric surveys between May 2022 and May 2023 (Fig. 2 and Table 2ESM). Regarding the subaerial part, we derived Digital Elevation Models (DEMs) from multiple platforms, including:

i) Single-Pass Interferometric Synthetic Aperture Radar (SP InSAR) airborne data collected on 12 September 2022 and 17 October 2022 over the entire island. In both surveys, the radar was installed onboard a Cessna 172, where the SP InSAR layout was obtained by mounting the different radar antennas on the strut of the right wing, as described in Natale et al. (2022) and Esposito et al. (2024). The DEM generation is based on the classical InSAR technique (Franceschetti and Lanari, 1999; Rosen et al., 2000; Esposito et al., 2023 and 2024), allowing to obtain a final DEM with a cell size of 1 m;

ii) photogrammetric method using PLÉIADES-1 tri-stereo satellite imageries collected on 22 August 2022, 24 October 2022 and 11 February 2023 over the entire island (for more details on the methodology refer to Di Traglia et al., 2020). The generated DEMs have a cell size of 1 × 1 m;

iii) photogrammetric method using images acquired by two UASs only on the SdF slope. The first vehicle was a DJI Matrice 300 RTK with Zenmuse P1 camera (full-frame CMOS 45MP sensor, 84° field of view and 24-mm focal length lens) and collected data on 20 May 2022, 15 October 2022, 15 December 2022, 1 February 2023, 22–23 May 2023 (for details on UAS data acquisition and processing refer to Civico et al., 2021 and 2024). The second vehicle is a Saturn Mini drone with a Canon IXUS 160 camera with 20 Megapixel resolution, which collected data on 18 October 2022 and 1 February 2023 (for details on UAS data acquisition and processing refer to Gracchi et al., 2022). The obtained DEMs have a cell-size of 0.5 cm. To correct the positioning of photogrammetric surveys, 15 points from a LiDAR (Light Detection And Ranging) survey carried out in 2012 were used as virtual GCPs (Ground Control Points) to co-register all the PLÉIADES-1 and UAS DEMs.

Regarding the submarine part, high-resolution bathymetric data were collected in two multibeam surveys performed on 31 May 2022 and 23 March 2023 onboard the small vessel Cheetah Marine (Idrosfera company) along the submarine portion of SdF. In both surveys, the multibeam R2Sonic was used, operating at a frequency range of 200–450 kHz. Data were DGPS-positioned, allowing obtaining sub-metric accuracy in the x-y plane and processed with hydrographic software, using daily sound speed profiles and patch test of transducers in the survey zone. Moreover, a hull-mounted sound speed sensor was used to update in real-time the sound velocity values close to the multibeam transducer. Tidal corrections were performed using data from the nearby tide gauge stations of Strombolicchio and Ginostra (www.mareografico.it, last access 23/12/2024). Random and organised acoustic noise was removed by applying geometrical and statistical filters as well as manual editing. The final DEM has a cell size of 3 m.

DEM-to-DEM co-registration was based on the minimization of the root mean square (RMS) error between two DEMs, using a custom-made algorithm (e.g., Favalli et al., 2018) and following the workflow outlined in Di Traglia et al. (2020). The morphological changes (slope erosion/accretion) and associated volumes (V) were calculated from each DEM of Difference (sensu Williams, 2012) according to the formula $V = \Sigma_i \Delta x^2 \Delta z_i$ (where Δx is the grid step and Δz_i is the height variation within the grid cell). The volume error was determined by the formula $ErrV = A\sigma\Delta Z$, where A is the investigated area, and $\sigma\Delta Z$ is the mean error of ΔZ (Favalli et al., 2010).

3.3. Slope stability analysis

A stability analysis of the SdF slope was performed using the 2D limit equilibrium method (LEM) implemented in the Slope Stability Analysis Program (SSAP; Borselli et al., 2011; Borselli, 2020), to assess the stress state of the slope and understand the failure mechanisms affecting volcaniclastic deposits. The factor of safety (FS) for potential slip surfaces was calculated using shear strength parameters derived from multiple failure criteria, following the same methodology used by Di Traglia et al. (2023a, b, and 2024), which successfully replicated past events. The geo-mechanical stratigraphy of the slope was represented by different geotechnical units (Fig. 4; Table 1):

1. Volcaniclastic infill: a shallow subaerial deposit of volcaniclastic material with rockfill-like properties. For this unit, failure was assessed using both the Generalised Hoek-Brown (GHB) criterion

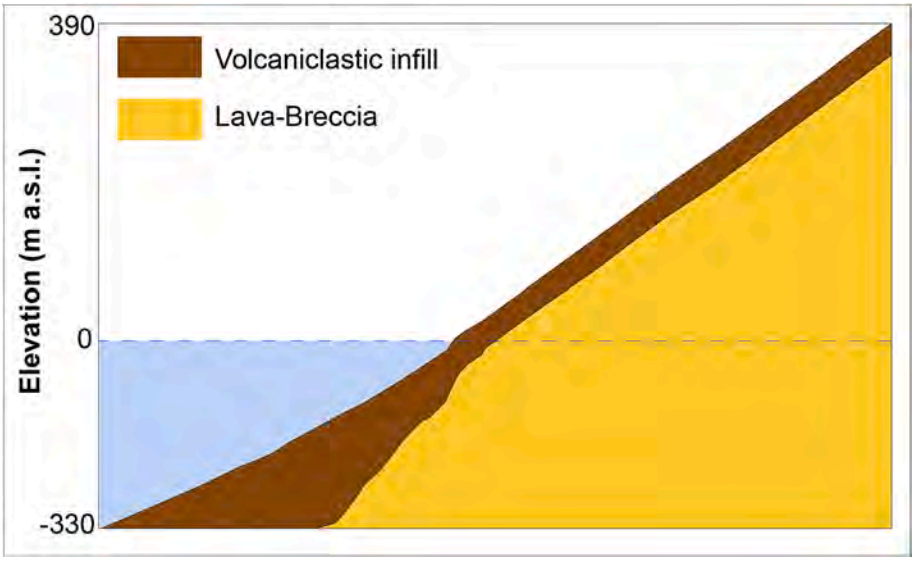

Fig. 4. Profile utilized for stability analysis, considering the distribution of volcaniclastic infill, the characteristics of which are detailed in Table 1, as well as the lava-breccia unit.

Table 1
Geomechanical parameters used in the LEM simulations.

Geomechanical parameters following GHB (Hoek et al., 2002)						
Layer	UCS (MPa)	GSI (–)	mi (–)	D (–)	γdry (kN/m3)	γsat (kN/m3)
Volcaniclastic infill	40	30	19	0	15	17
Lava-Breccia	40	30	19	0	19	22

Barton and Kjærnsli (1981) Criterion following parametrization of Lunardi et al. (1994) and Barton (2013)							
Layer	JRC (°)	JCS (Mpa)	φr (°)	L0 (m)	L (m)	β (°)	Δβ(°)
Volcaniclastic infill	20	10	32.00	1.00	150.00	40.00	20.00

(Hoek et al., 2002; Hoek and Brown, 2019; Haep et al., 2020) and the Barton-Kjaernsli (B—K) nonlinear envelope (Barton and Kjærnsli, 1981; Barton, 2013), reflecting its local interaction with the underlying lava-breccia.

2. Lava-breccia unit: a deeper lithostratigraphic layer of 35–65 % lava alternating with breccia, representative of the deeper volcanic structure. The GHB criterion was also applied to this unit, used here as a geotechnical lower boundary.

This stability analysis used detailed topographic data derived from Pleiades-1 DEM and multibeam bathymetry.

4. Results

4.1. Morphological changes occurred along the SdF slope

The comparison of topographic and bathymetric surveys realized in May 2022 and March–May 2023 (the latter for the marine and subaerial slopes, respectively) shows that the main morphological changes within the analysed eruptive period occurred in the central part of SdF (Figs. 5 and 6).

The 2022–2023 DEM of Difference (Fig. 5) shows an impressive continuity between slope erosion and accretion along the submarine and subaerial parts of SdF. Erosion is largely overwhelming accretion (i.e., 20 times larger) along the subaerial slope, accounting for estimated volumes of ~2 × 10^6 m^3 and ~92 × 10^3 m^3, respectively (Table 2). On the contrary, accretion dominates over erosion (i.e., almost the double) along the submarine slope of the SdF, with estimated volumes of ~1 × 10^6 m^3 and ~660 × 10^3 m^3, respectively (Table 2). Two main areas of accretion (A1 and A2 in Fig. 5) are recognizable in the lower subaerial slope and in facing marine areas.

A1 extends between ~100 m asl and ~200 m bsl and morphologically matches the development of a steep-sided ridge (yellow polygon in Fig. 6b, see also profiles T3, B1 and B2 in Fig. 7), characterized by multiple slope breaks and local slope gradients up to 80°. The thickness of A1 markedly increases in the coastal and nearshore areas, reaching a maximum value of 17 m (profiles T3 and B1 in Fig. 7), accounting for an estimated volume of ~220 × 10^3 m^3, ~70 % of which emplaced in the marine area (Table 2).

A2 is the largest accretion area between 80 m bsl and 400 m bsl (limit of the bathymetric survey, Fig. 5). A2 has an average thickness of 5.5 m (locally up to 13 m, profiles B2 and B3 in Fig. 7), accounting for an estimated volume of ~860 × 10^3 m^3 (Table 2). A2 still shows a relevant thickness at 400 m bsl (Fig. 5), indicating that it extends seaward. A2 shows an overall fan-shaped morphology (pale brown polygon in Fig. 6b), formed by the juxtaposition/coalescence of smaller fans.

Minor slope accretions are recognizable along the SW part of the central sector both in the submarine (A3 in Fig. 5 and profile B1 in Fig. 7) and subaerial slope (A4 and A5 in Fig. 5 and profile T1 in Fig. 7). Area and volume estimates are given in Table 2.

Slope erosion is mainly recognizable in the subaerial slope (E1 in Fig. 5), where a narrow and steep-sided canyon developed through time (Fig. 6b, more details in Section 4.1.1) and secondarily along the coastal and marine areas (E2-E5 in Fig. 5). E2 is a well-defined incision at the foot of the subaerial slope (profile T3 in Fig. 7); its submarine part mobilized up to 10 m of thickness in the first 100–200 m bsl (Fig. 5), accounting for a volume of ~430 × 10^3 m^3 (Table 2). The submarine part of E2 is morphologically characterized by two landslide scars in the first 100–200 m bsl, merging downslope in an erosive channel (profiles B1, B2 and B3 in Fig. 7). E3 is mostly submarine, with a maximum mobilized thickness of 12 m (Fig. 5 and profile B1 and B2 in Fig. 7), accounting for a volume of ~180 × 10^3 m^3 (Table 2). E3 is morphologically associated with the development of small-scale (~60 m in diameter) landslide scars in the first 100 m bsl that evolve downslope in elongated and narrow erosive channels (Fig. 6b). The corresponding

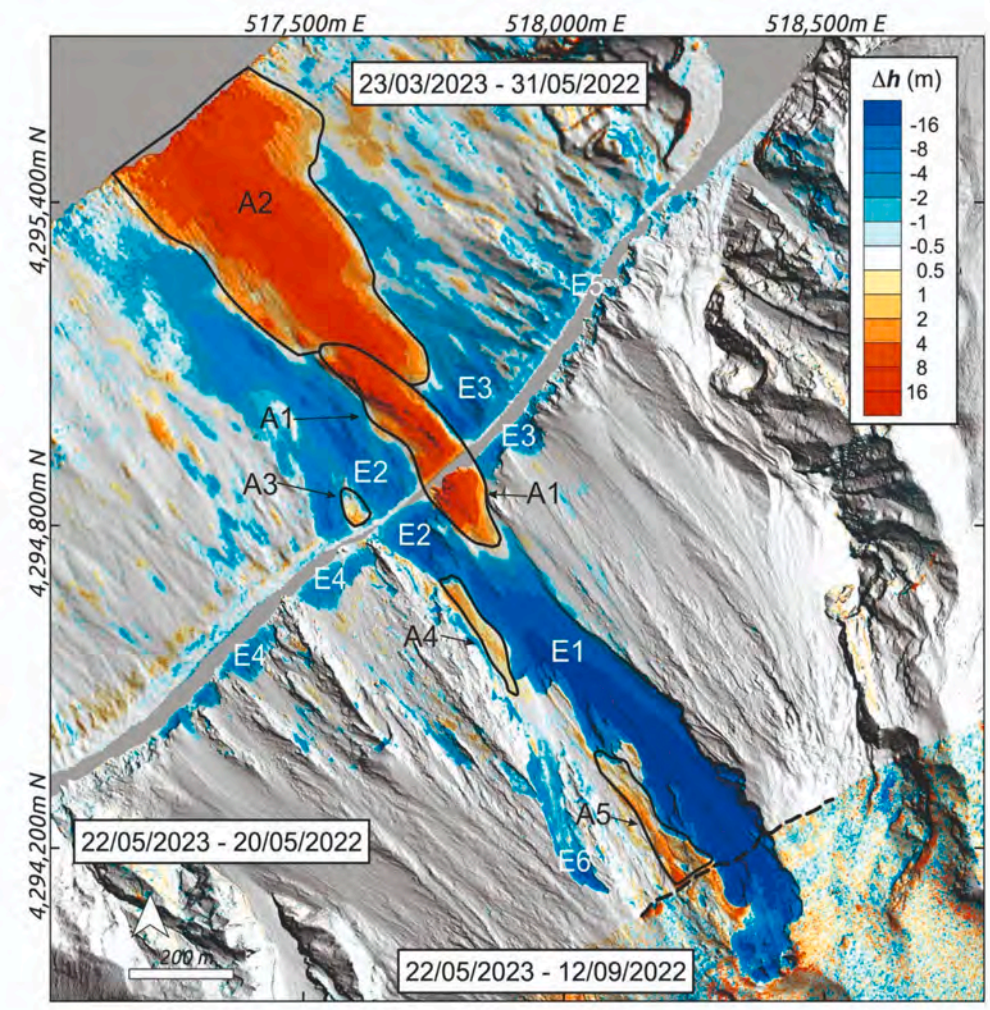

Fig. 5. DEM of Difference over the entire monitoring period, showing the main topo-bathymetric changes on the SdF slope. E1-E6 and A1-A5 are areas characterized by slope erosion and accretion, respectively (see text for details).

coastal sectors, facing E2 and E3, are affected by shallow erosion (Fig. 5 and profile T3 in Fig. 7). Minor areas with slope erosion are present along the SW and NE coastal/nearshore sectors of SdF (E4 and E5 in Fig. 5) as well as in the upper SW sector of SdF (E6 in Fig. 5).

4.1.1. Short-term morphological evolution of the subaerial slope

Repeated topographic surveys through UASs were performed between May 2022 and May 2023 period, enabling to monitor with high detail the morphological evolution of the subaerial slope (Figs. 8–11), which can be divided in three different stages:

a) the first stage was dominated by a marked erosion throughout the central part of SdF, up to ~650 m asl (upper limit of the survey, Fig. 8a), with an average mobilized thickness of ~21 m (locally up to ~45 m), accounting for an estimated volume of ~1.9 × 10^6 m^3 (Table 3). This stage mostly occurred between 9 and 15 October 2022, when a series of PDCs initially related to the 9 October crater rim failure and then to the crumbling of the lava front overflows were observed (Fig. 3 and Table 1ESM). The slope erosion was morphologically associated with the development of a V-shaped, steep-sided and narrow (100 m wide at maximum) canyon that reached its maximum depth incision during this period (Figs. 9a and 10a).

The lower part of the canyon was generally less incised and showed areas of slope accretion along the coastal sector associated with the development of steep-sided ridges (Figs. 8a and 11a). A main slope accretion was recognized along the SW part of the canyon (ELO in Figs. 8a and 11a), matching the location of early lava overflows seen from UAS images (Fig. 3b).

Once the PDCs activity stopped, the canyon floor was partially filled by lava overflows as recorded in the 18 October 2022–15 October 2022 Dem of Difference (Figs. 8b, 9b and 10b and Table 3). A small part of this slope accretion occurred at the base of the NE canyon flank and was linked with the deposits of the retrogressive erosion of the canyon flank (Fig. 10b and Table 3).

b) The second stage of canyon evolution was mainly related to the NE crater rim failure that occurred on 4 December 2022, which breached half of the NEC and produced multiple PDCs for a few hours (Fig. 2 and Table 1ESM). The 16/12/2022–18/10/2022 DEM of Difference evidenced significant slope erosion at elevation > ~600 m asl (on average 16 m, locally up to 30 m in Fig. 8c). Slope erosion was related both to the NEC collapsed area and retrogressive erosion of the previous canyon head (Figs. 8c and 9c, and Table 3), with the development of arcuate and nested landslide scars. At elevation <600 m asl, the canyon floor was dominated by slope accretion (Figs. 8c and 10c, and Table 3) due to the emplacement of multiple lava overflows fed from the breached NEC, whose effusive activity lasted until 8 December 2022 (Fig. 2).

A maximum thickness of 15 m was recognized in the lower slope, where the stacking of lava flows formed a steep-sided ridge, before enlarging in the coastal sector to build a small lava delta (Figs. 8c and 11b). Minor slope accretion was present at the base of the canyon flanks due to deposits associated with retrogressive erosion (Figs. 10c and 11b,

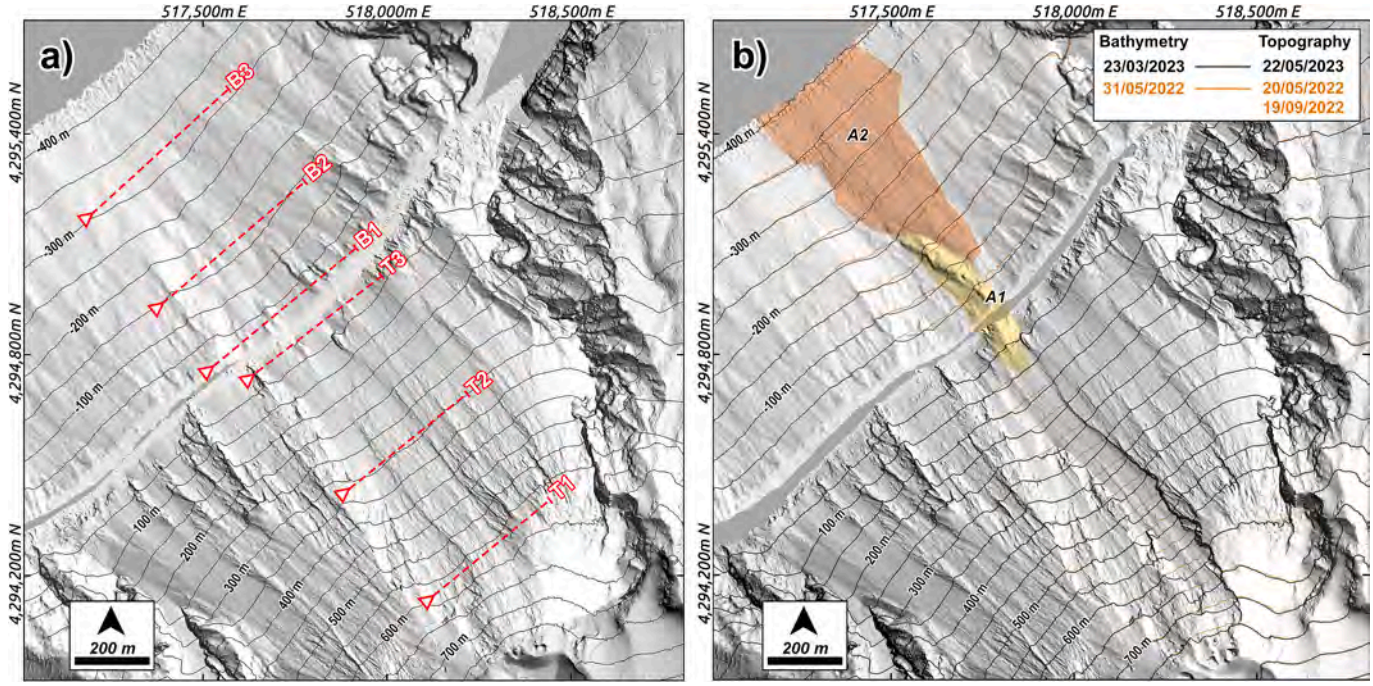

Fig. 6. Shaded reliefs and isobath maps for the May 2022 DEM (a) and comparison with the isobath-contour map of the March/May 2023 submarine and subaerial surveys, respectively (b), to evidence the main morphological changes occurred during the studied eruptive period. The main slope accretion areas A1 and A2 are evidenced in yellow and pale brown, respectively. The red dashed lines in (a) are the traces of the topographic and bathymetric sections shown in Figs. 7, and 9–11.

Table 2
Areas and volumes (with associated errors) computed for the main areas with morphological changes shown in Fig. 5. Note that E1 "above/below 650 m asl" refers to the dashed black line in Fig. 5.

2022–2023 DEM of Difference	Area (m^2)	Vol (m^3)	Vol_error (m^3)
E2	126,378	−435,912	±56,563
E3	79,767	−178,573	±35,701
E4	44,658	−44,473	±19,988
Total submarine erosion	250,803	−658,958	±112,252
A1	27,531	156,340	±12,322
A2	155,187	861,541	±69,457
A3	1412	1315	±632
Total submarine accretion	182,718	1,019,196	±82,411

2022–2023 subaerial changes	Area (m^2)	Vol (m^3)	Vol_error (m^3)
E1 (below 650 m)	117,373	−1,496,444	±22,178
E1 (above 650 m)	29,616	−361,984	±28,356
E2	11,074	−90,792	±2092
E3	7954	−28,853	±1503
E4	9214	−24,156	±1741
E5	6999	−20,091	±1322
E6	18,377	−55,214	±3472
Total subaerial erosion	200,607	−2,077,534	±60,665
A1	13,370	66,842	±2526
A4	6346	6616	±1199
A5	11,539	18,945	±2180
Total subaerial accretion	31,255	92,403	±5906

and Table 3). Besides lava delta formation, the coastal sector was dominated by slope erosion, mostly occurring outside the subaerial canyon (Figs. 8c and 11b). The maximum slope deepening in the coastal sector (up to 15 m) was just SW of the lava delta, forming a marked coastal scar that cut back up to ~100 m asl (coastal erosion "ELO" in Figs. 8c and 11b, and Table 3). This area was previously characterized by early lava overflows emplaced during the initial evolution of the canyon (Figs. 3b, 8a, and 11a).

c) The last stage of canyon evolution occurred from 16 December 2022 to 22 May 2023, characterized by normal explosive activity interrupted by different episodes of lava overflows from the crater rim alternated with major explosions (Fig. 2 and Table 1ESM). During this period, the NEC collapsed area and the canyon floor were dominated by slope accretion, with a thickness of several meters as recorded in the DEMs of Difference for 1 February 2023–16 December 2022 and 22 May 2023–1 February 2023 (Fig. 8d and e, and Table 3). On the contrary, slope erosion occurred along the upper part of the canyon flanks and the coastal area as well (Fig. 8d and e, Table 3). In the former case, slope erosion mobilized an average thickness of ~5 m (locally up to 20 m), leading to a progressive widening of the canyon (Fig. 9d and e). In the latter case, slope erosion mostly affected the SW part of the canyon and the seaward portion of the previously built lava delta (Fig. 11c and d). The 22 May 2023–1 February 2023 DEM of Difference also evidenced patchy coastal accretion linked with erosion upslope (Fig. 11d).

4.2. Slope stability analysis

The stability analysis of the SdF slope indicates that the coastal and nearshore areas, extending to depths of around 100 m, are the most unstable (see Fig. 12). Additionally, a thin-skinned instability zone (cf. Ebmeier et al., 2014) was identified between 500 and 200 m above sea level. These sectors consistently exhibit FS values approaching 1, indicating widespread instability along the subaerial slope and more localised instability within the coastal zone, particularly in the submarine sector. The analysis has identified potential detachment areas along the coastline capable of mobilizing deposits some tens of metres thick with FS values below 1. These results align with natural coastal erosion processes driven by wave action, mobilizing slope thickness up to 10 m (Kokelaar and Romagnoli, 1995; Casalbore et al., 2022; Di Traglia et al., 2022) as well as with larger (thick up to 20–30 m) instability processes caused by PDCs and lava flows entering the sea (Casalbore et al., 2022; Di Traglia et al., 2022). The stability models make it possible to identify the source areas of deposit-derived PDCs along the subaerial slope of the SdF. This is the result of the failure and mixing of lava overflows and volcaniclastic deposits.

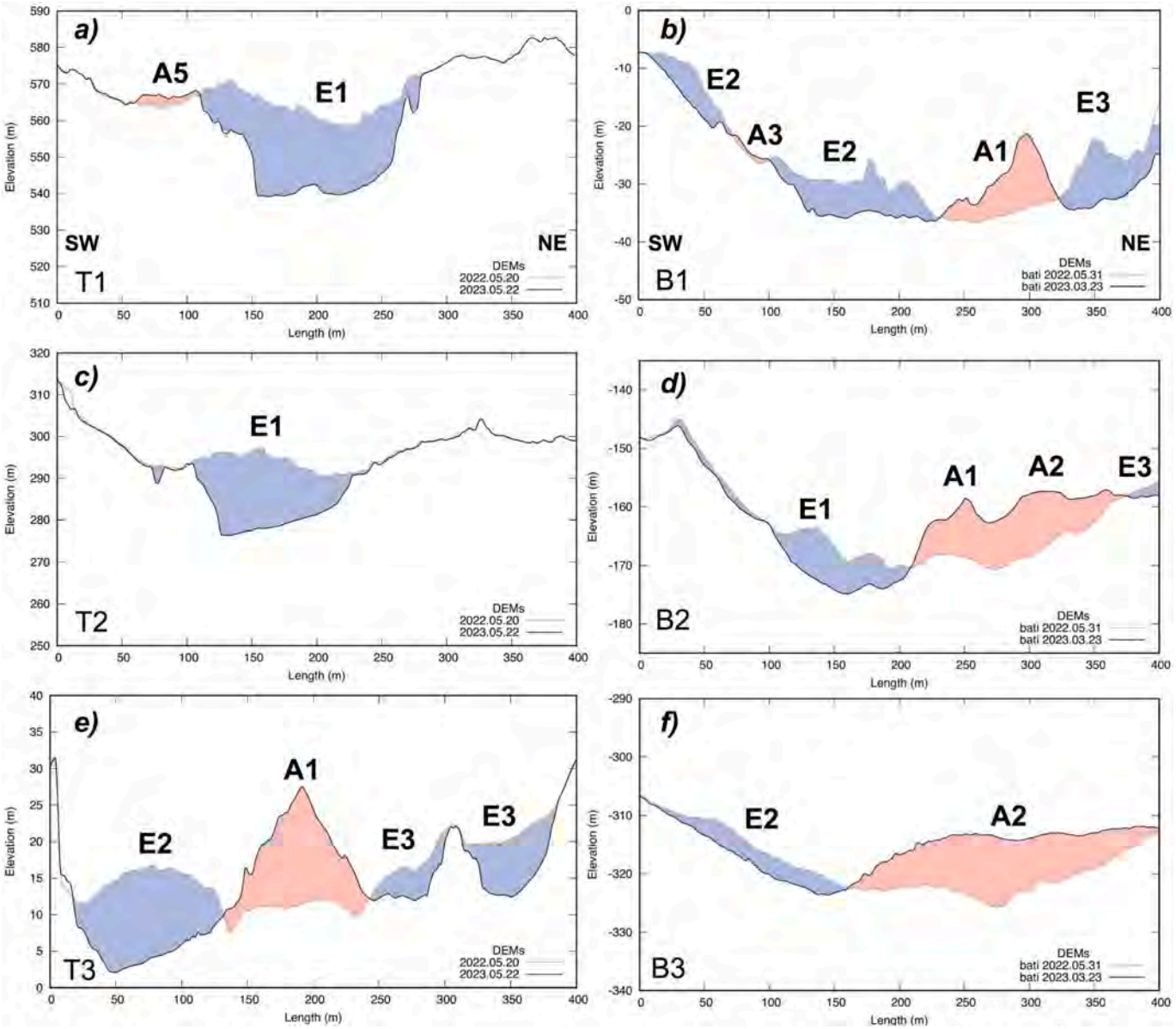

Fig. 7. Topographic (T1-T3) and bathymetric (B1-B3) profiles showing slope erosion (in blue) and accretion (in red) over the entire eruptive period; location in Fig. 5. The labels E1–3 and A1–2 are referred to Fig. 5.

5. Discussion

5.1. Processes controlling canyon formation and evolution

A main role in the canyon formation is due to PDCs, whose erosive potential along the SdF slope is supported both by previous volcanological observations through real-time cameras (Calvari et al., 2022; Di Traglia et al., 2022) and studies of the related ash-cloud deposits (Re et al., 2022). The componentry analysis of the deposits associated with the May 2021 PDC revealed a preponderance of remobilized material ingested during its flowing along the SdF slope (Re et al., 2022). Similar observations have been reported for other PDCs deposits elsewhere (e.g., Calder et al., 2000; Cole et al., 2005; Lube et al., 2007; Sarocchi et al., 2011; Brand et al., 2014), which can include up to 50 % in weight of non-juvenile material, such as for the 2006 eruption at Tungurahua volcano in Ecuador (Bernard et al., 2014). In the latter example, PDC bulking due to slope erosion mostly occurred on the upper and steeper ($> 25°$) part of the volcanic flank, in agreement with the marked slope erosion (Fig. 5) observed on the very steep (on average 35°) subaerial SdF flank. However, erosion due to PDCs flowing along the SdF slope (Fig. 13a), as occurred during the July–August 2019 paroxysms (Di Traglia et al., 2022) or the May 2021 crater rim collapse (Casalbore et al., 2022), did not produce yet the subaerial canyon, indicating that a more complex and peculiar chain of events happened during the 2022 eruptive period (Fig. 13). Based on the available data, we can reconstruct that the canyon formation started with the development of a large coastal landslide on 9 October 2022 (Fig. 3b and 13b), which rapidly evolved upslope through retrogressive slope failures within a single week (Fig. 13 c, d). This slope evolution followed the upslope migration of the lava flow/PDCs transition point and stopped with the ending of PDCs (Fig. 3c, d), suggesting a feedback loop between the development of retrogressive failures and PDCs erosion. This is likely due to the acceleration of PDCs at the slope break formed by the landslide scar, which favoured the formation of further retrogressive slope failure due to the shear stress applied by PDCs over this area and/or to an increase of the PDC's erosive activity downslope. In both cases, the retrogressive erosion upslope led to the formation of a narrow proto-canyon within SdF, which acted as a topographic constraint for the successive PDCs,

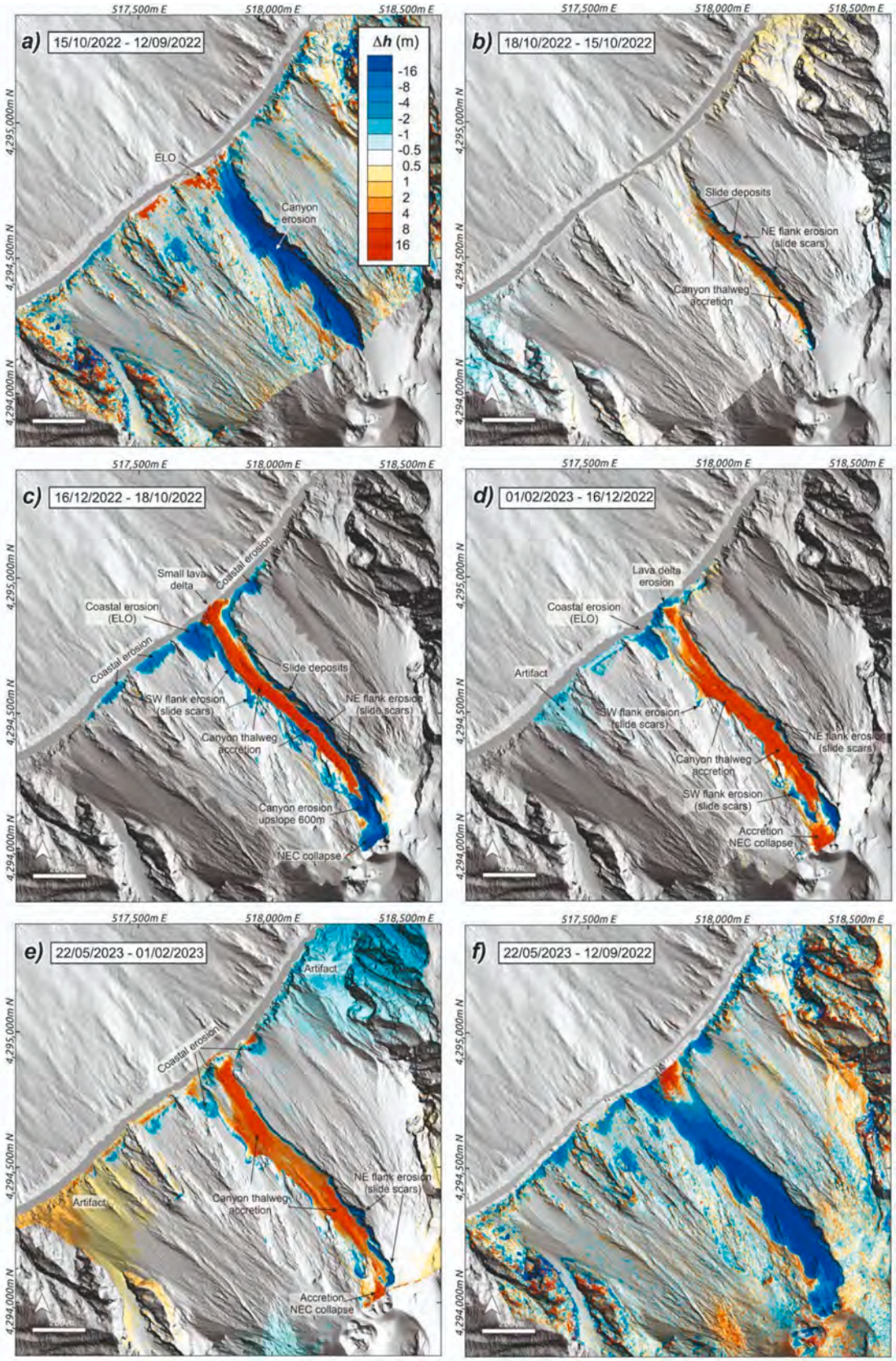

Fig. 8. a-e) Difference maps of UAS surveys on the SdF, showing the morphological evolution of the subaerial canyon and surrounding areas. f) Difference map computed over the entire period shown by previous images. ELO = Early Lava Overflows; NEC = North-East Crater.

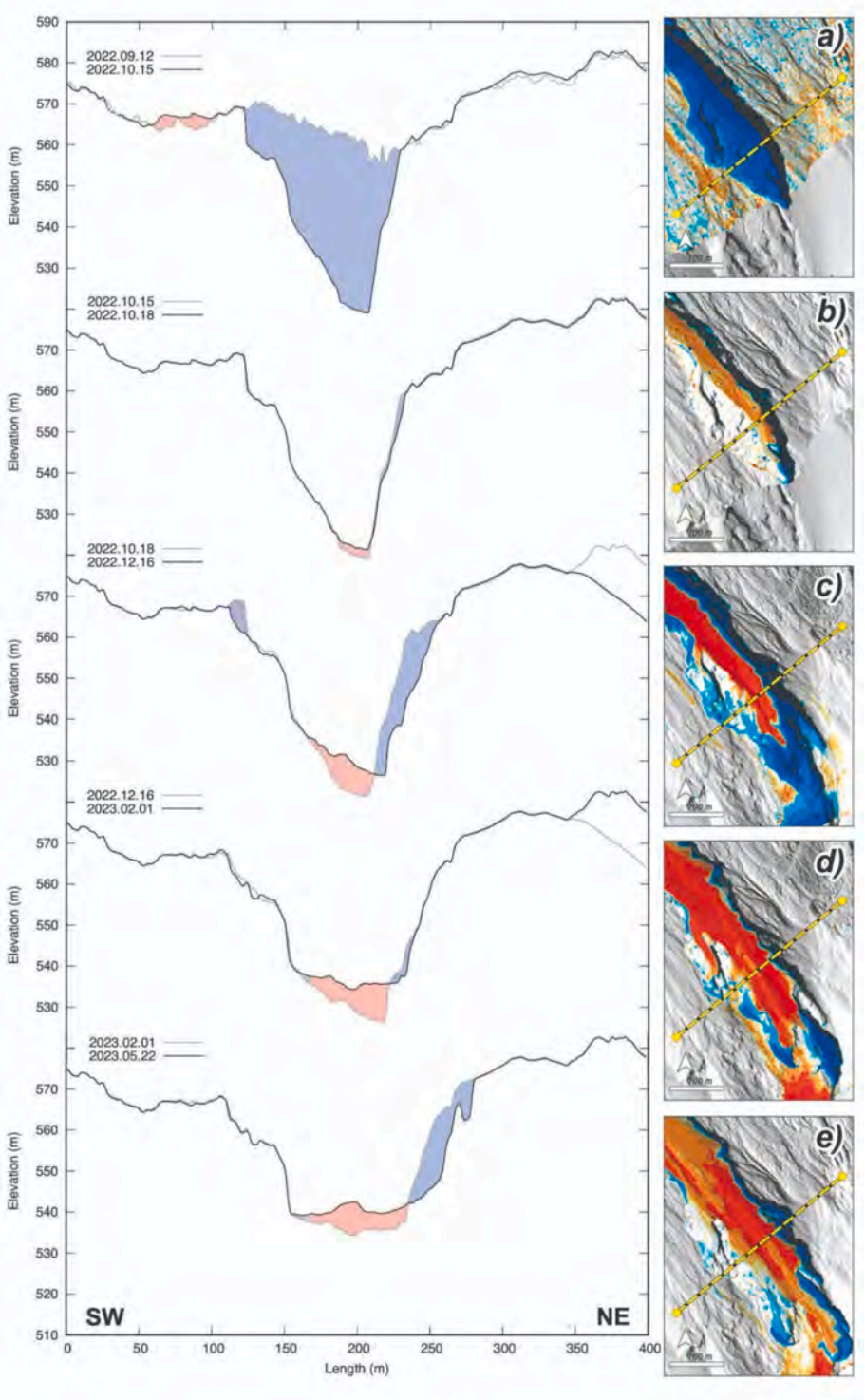

Fig. 9. Topographic profiles showing the morphological evolution through time of the upper part of the canyon (location is indicated by a yellow dotted line in maps on the right, see also profile T1 in Fig. 6a). On the right, the zoom of the difference map refers to the corresponding period. Blue and red areas are slope erosion and accretion, respectively.

further increasing their basal shear stress and related erosive capacity, as reported during the 1980 eruption at Mount St. Helens (Brand et al., 2016).

Regarding the formation of the initial coastal landslide scar, we also propose the occurrence of retrogressive evolution from a shallow-water landslide (Fig. 13a), similar to what happened (at larger spatial scale) during the 30 December 2002 tsunamigenic landslides (Chiocci et al., 2008a). Unfortunately, the detailed succession of events in the marine and coastal area in October 2022 cannot be supported by the bathymetric surveys, which were realized several months after the coastal slide, showing only seafloor accretion due to entrance into the sea of later lava overflows in the original scar (Fig. 5). However, slope stability analysis indicates that the nearshore (down to 100 m bsl) was one of the most critical areas of SdF (Fig. 12), potentially leading to the development of a rotational landslide remobilising material up to 30 m thick, especially if loaded by lava overflows and/or the entrance into the sea of

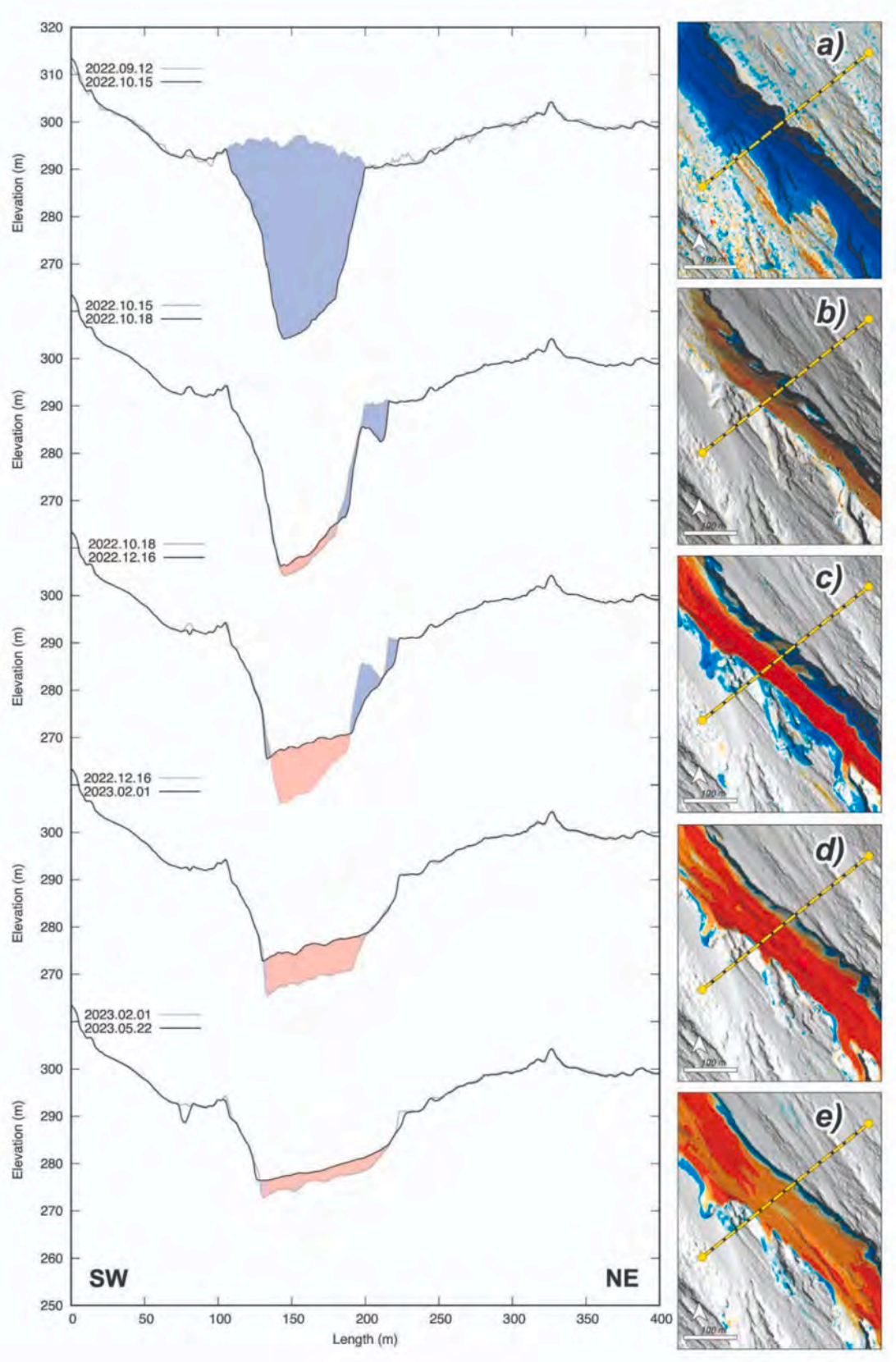

Fig. 10. Topographic profiles showing the morphological evolution through time of the median part of the canyon (location is indicated by a yellow dotted line in maps on the right, see also profile T2 in Fig. 6a). On the right, the zoom of the difference map refers to the corresponding period. Blue and red areas are slope erosion and accretion, respectively.

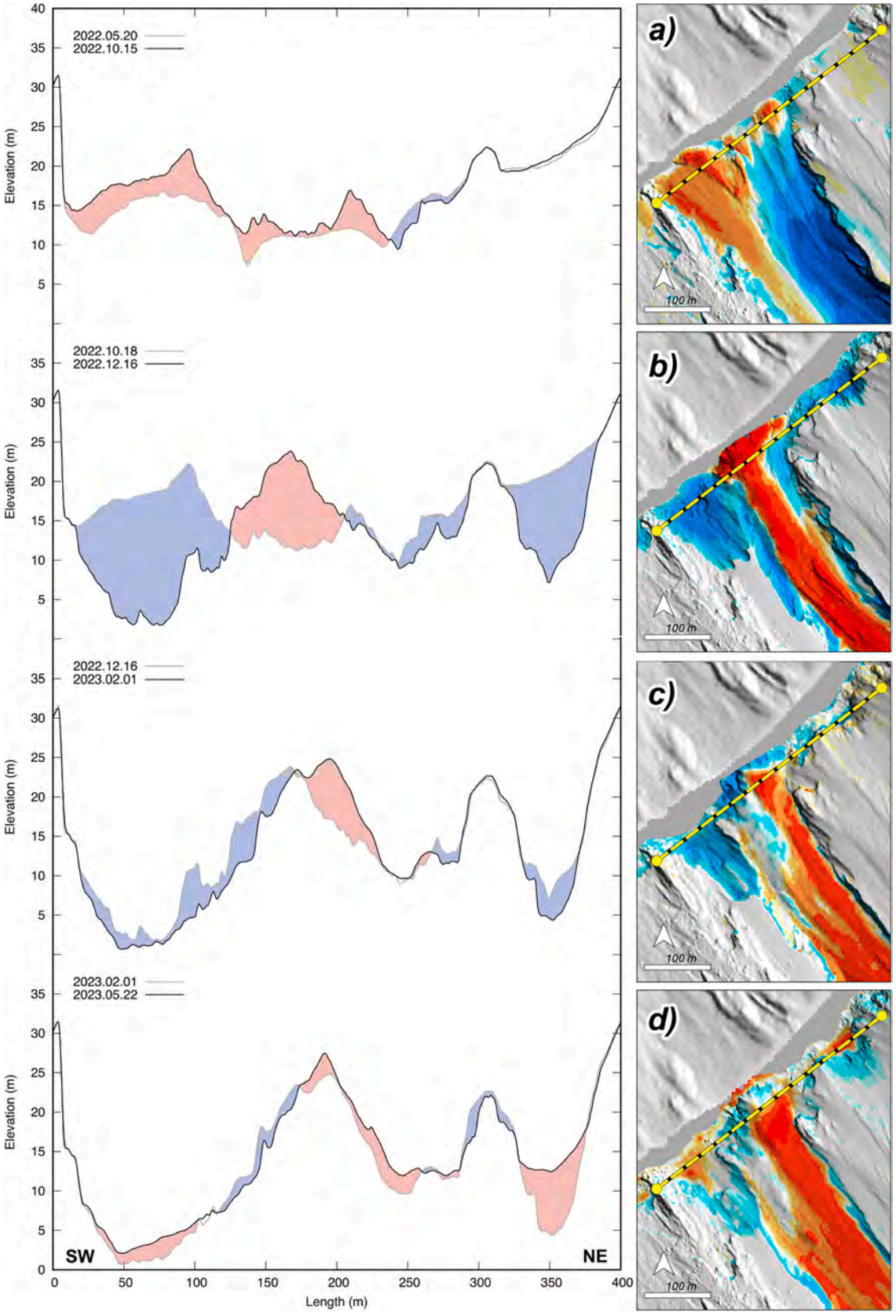

Fig. 11. Topographic profiles showing the morphological evolution through time of the coastal part of the canyon (location is indicated by a yellow dotted line in maps on the right, see also profile T3 in Fig. 6a). On the right, the zoom of the difference map refers to the corresponding period. Blue and red areas are slope erosion and accretion, respectively.

Table 3
Areas and volumes (with associated error) computed for the short-term morphological changes shown in Fig. 8 in the subaerial SdF. ELO = Early Lava Overflows; NEC = North-East Crater.

DEM of Difference	Subaerial short-term changes	Area (m^2)	Vol (m^3)	Vol_error (m^3)
15/10/22–12/09/22	Erosion (canyon)	92,627	−1,906,425	±58,089
18/10/22–15/10/22	Erosion (canyon flanks)	18,612	−52,071	±2085
18/10/22–15/10/22	Accretion (canyon thalweg)	28,923	45,964	±3240
16/12/22–18/10/22	Erosion (summit collapse)	7179	−93,030	±814
16/12/22–18/10/22	Erosion (canyon upslope 600 m)	10,559	−164,348	±1197
16/12/22–18/10/22	Erosion (canyon flank)	65,677	−310,897	±7448
16/12/22–18/10/22	Erosion (coastal area, ELO)	12,685	−90,730	±1439
16/12/22–18/10/22	Erosion (external coastal areas)	27,300	−129,525	±3096
16/12/22–18/10/22	Total subaerial erosion	116,221	−695,500	±13,180
16/12/22–18/10/22	Accretion (canyon thalweg and coast)	47,051	342,913	±5336
01/02/23–16/12/22	Erosion (canyon flanks)	28,064	−121,323	±4256
01/02/23–16/12/22	Erosion (coastal area)	13,329	−59,193	±2021
01/02/23–16/12/22	Total subaerial erosion	41,393	−180,517	±6277
01/02/23–16/12/22	Accretion (canyon thalweg)	69,395	344,434	±10,523
01/02/23–16/12/22	Accretion (NEC collapse)	7769	50,190	±1178
01/02/23–16/12/22	Total subaerial accretion	77,164	394,624	±11,702
22/05/23–01/02/23	Erosion (canyon flank)	53,890	−127,599	±9189
22/05/23–01/02/23	Accretion (canyon thalweg)	96,821	295,743	±16,509

PDCs. The key role played by PDCs in triggering submarine slope instabilities at SdF was already reported both for the 3 July 2019 and 21 May 2021 events (Di Traglia et al., 2022; Casalbore et al., 2022). Moreover, a similar slope evolution can be envisaged for the 4 December 2022 PDCs, which are responsible for the generation of slope failures in the coastal (Fig. 8d) and facing marine sectors (E2–4 in Fig. 5).

As the size and position of the 9 October 2022 coastal landslide are concerned, they were mainly controlled by litho-morphological limits due to previous lava flows (Figs. 13 and 14). The NE limit of the landslide scar matches a rocky outcrop associated with the emplacement of the large 2007 lava flow field (Fig. 14b, c; Marsella et al., 2012), which is not affected by any topographic variations during the entire canyon evolution (Fig. 14d). The role of the 2007 and (partly overlapping) 2014 lava flow fields in controlling the later canyon evolution is also demonstrated by the fact that they acted as a main morpho-lithological limit for canyon widening through time (Figs. 8, 9, 10, 13, 14c, d). Differently, the SW limit of the 9 October 2022 coastal landslide matches the remnant of a much smaller morphological ridge formed by the 19 May 2021 lava overflows (Fig. 14a, b, c; Casalbore et al., 2022), and it was totally removed after the 4 December 2022 PDCs (Figs. 8c and 14d).

Beside the gradual widening, the morphological evolution of the canyon was mainly characterized by its progressive filling due to lava overflows from the crater rim, which reached a maximum thickness in the coastal area (Figs. 8, 9, 10) due both to the marked decrease of slope gradients and difficulties of lava flows in penetrating the sea-land interface (e.g., Tucker and Scott, 2009; Stevenson et al., 2012; Bosman et al., 2014). The only exception to this overall canyon filling was observed just after the 4 December 2022 crater rim collapse, which led to the last stage of retrogressive upslope evolution of the canyon (Figs. 8c, 13f and 14d). In this case, the presence of 10–20 m high, subvertical slope breaks due to retrogressive slope failures controlled the erosive behaviour of lava overflows in the upper part of the canyon, as testified by the DEM of Difference (Figs. 7c and 8c) and volcanological observations (Section 2.1). Efficient thermo-mechanical erosion by small-volume basaltic-andesite lava flows was similarly reported on the steep-sided Momotombo volcano in Nicaragua (Gallant et al., 2020) and Sangay volcano in Ecuador (Bedón et al., 2024). In such cases, lava flows incised into the pyroclastic substrate down to 30 m, indicating that *syn*-eruptive erosion may represent a significant morphogenetic process on steep-sided volcanoes that are predominantly composed of layered pyroclastic successions, such as at Stromboli.

5.2. *Canyon as a preferential conveyor of volcanics to the sea and implications for geohazard assessment*

The prevalent seafloor accretion recognized along the SdF slope down to 400 m bsl (Fig. 5) can be related to two main inputs: 1) deposits associated with the PDCs generated during the 9 October 2022 and 4 December 2022 crater rim collapses and/or 2) the funnelling into the sea of the large amount of lava overflows and volcaniclastic materials from ordinary explosive activity at the summit craters (especially the breached NEC) during the eruptive period (Table 1ESM). The first contribution can be considered low or negligible because of the steep gradients (> 20°, locally up to 40°) along this submarine part of the SdF, promoting an erosive behaviour of PDCs as observed just after the 3 July 2019 paroxysm (Di Traglia et al., 2022). The erosive behaviour of PDC's (or better of the related volcaniclastic density currents, sensu Clare et al., 2023) in marine environments seems to occur on smaller slope gradients with respect to their subaerial counterparts (Section 5.1) as suggested by: a) previous studies of PDCs entering the sea at Montserrat in 2006 (Trofimovs et al., 2006), where about the 30 % of the deposits accumulated in the proximal sectors on slope gradients <11° and the remaining 70 % transported 40 km away by sedimentary gravity flows on slopes <2°; b) the critical gradient of 12° for volcaniclastic density currents to become erosive in a fully submarine setting as observed for the 2022 eruption of Hunga volcano (Clare et al., 2023); c) the threshold of 8°-15° identified for the generation of large- and small-scale upper flow regime bedforms along the submarine flanks of insular volcanoes (Casalbore et al., 2021). The marked erosive or by-passing behaviour of PDCs along the surveyed sector of the submarine SdF is also supported by the comparison of the total mobilized volumes along the SdF slope over the monitoring period (Table 2), showing that erosion (~2.7 × 10^6 m^3, ~76 % of which in the subaerial slope) is more than the double than slope accretion (~1.1 × 10^6 m^3, ~92 % of which in the submarine slope). Furthermore, this volumetric difference is underestimated, considering that the canyon was progressively filled by lava overflows from the crater rim (Figs. 7–10), accounting for an additional volume of ~1 × 10^6 m^3.

Most of the recognized seafloor accretion is related to the

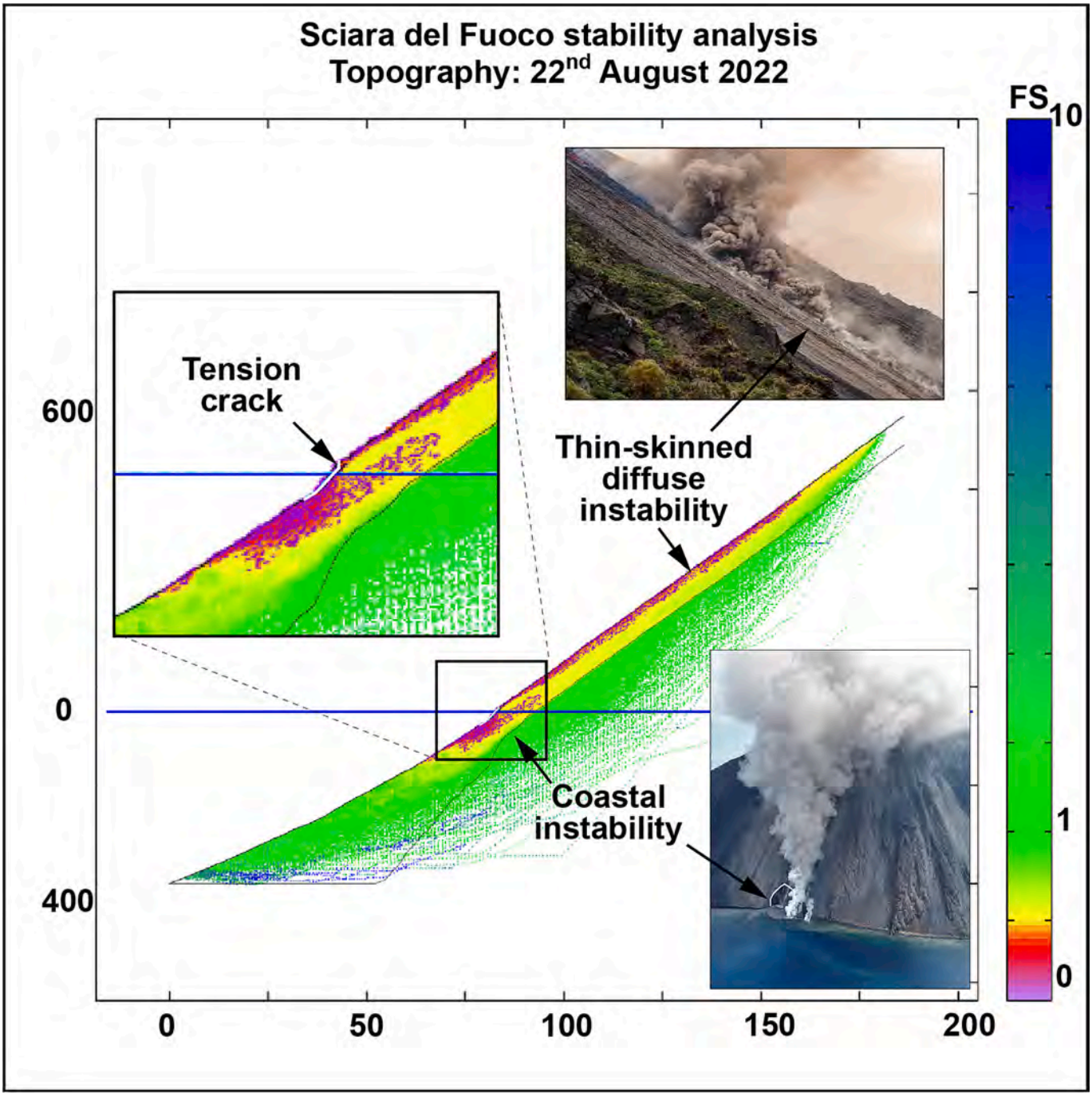

Fig. 12. Results of the LEM stability analysis obtained with slope stability LEM software SSAP (Borselli, 2023). The insets allow comparison between the modelled zones of lower stability and the field observations recorded during the events of 9 October 2022.

development of a large fan-shaped feature (A2 in Fig. 5 and pale brown area in Fig. 6b), whose complete extension goes beyond the limit of the bathymetric survey. Despite the underestimated size and volume, this fan-shaped feature is much larger than all the previously detected ones over the last 20 years (e.g., Casalbore et al., 2020 and 2022), pointing out a key role played by the unprecedented canyon formation in funnelling volcanics to the sea. This large fan can be interpreted as due to the seaward transport, through submarine gravity flows, of material accumulated in the coastal and nearshore sectors from: i) the brecciation of lava overflows, especially at the coastline during stages of low effusion rates, ii) the deposition of the coarsest-grained fraction of the PDC entering into the sea, as suggested by experimental observations (Freundt, 2003), iii) small but countless avalanches from the steep subaerial SdF, reaching the coastal and nearshore sectors. The lack of a current connection between the A2 fan apex with respect to the canyon mouth (Figs. 5 and 6) can be explained by the combination of two causes: a) the progressive NE-ward shift of the entry points of lava overflows through time (Fig. 11), and b) the later superimposition of the steep-sided ridge A1 over the original A2 fan during the last eruptive stage (Figs. 5 and 6b, yellow area). A1 is similar in shape to the morphological ridges emplaced during the 2007 and 2014 large lava deltas at Stromboli (Bosman et al., 2014; Casalbore et al., 2021) or to the smaller ridge formed by lava overflows in the aftermath of the 21 May crater rim collapse (Fig. 12a; Casalbore et al., 2022). All these ridges are characterized by different sub-vertical slope breaks along their flanks, suggesting the presence of coherent lava flows alternated with chaotic

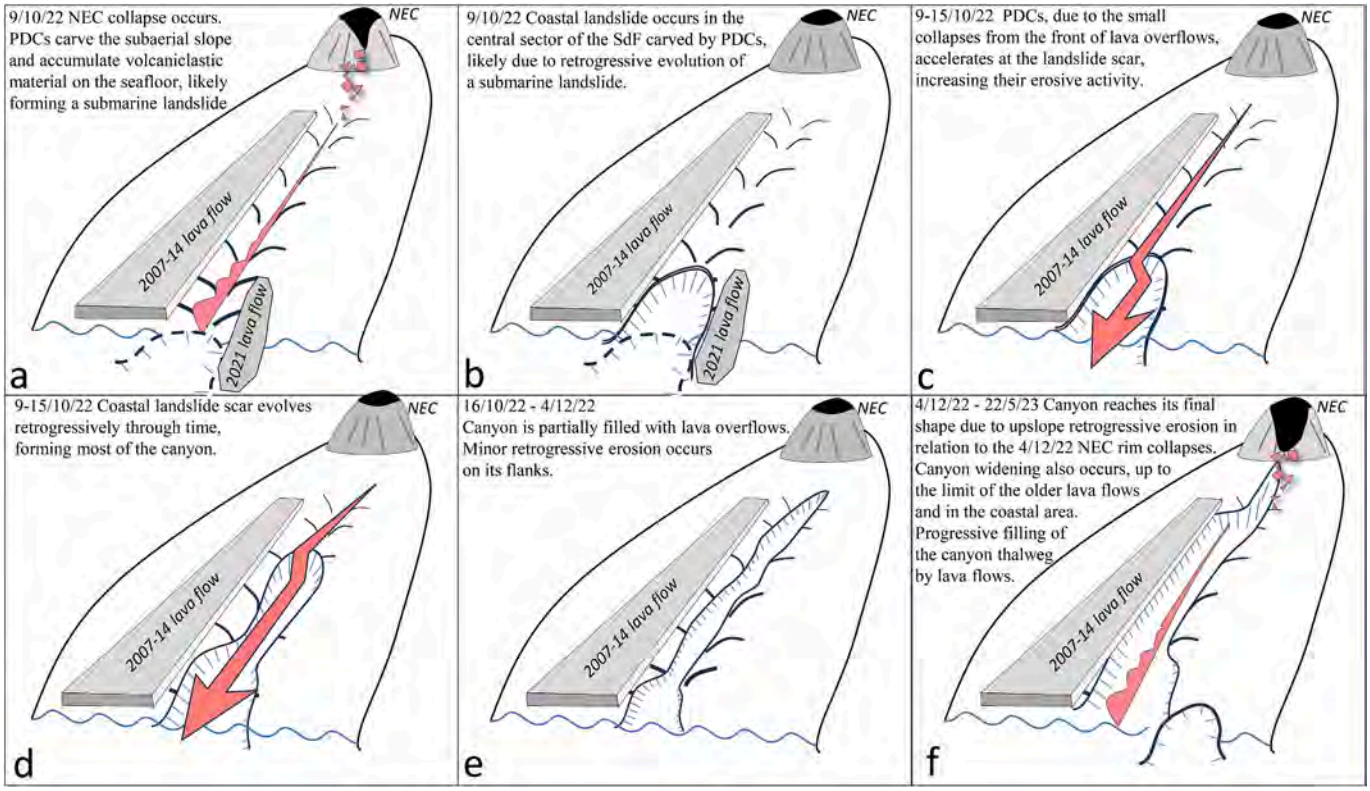

Fig. 13. Simplified sketch (not in scale) showing the morphological formation and evolution of the subaerial canyon in the central part of the SdF from the crater area to the coastline (undulated light-blue line) and facing nearshore sector, during the 2022–2023 eruptive period; for details refer to the text.

breccias, as observed in "lobe hyaloclastites" of ancient 'a'ā lava deltas (Smellie et al., 2013). We can also speculate that A1 formation mostly occurred after the 4 December 2022 crater rim failure, because if present, this ridge would have been mostly dismantled by the entrance into the sea of the 4 December 2022 PDCs, similarly to what happened to the smaller ridge formed by the May 2021 lava overflows (Figs. 5 and 13).

The reconstructed morphological evolution of the SdF slope in response to different eruptive dynamics, together with the estimation of potential volumes (such as the A1 ridge or the A2 fan-shaped features, Table 1) that can be remobilized in case of a further occurrence of PDCs along SdF, provide input parameters for a proper modelling of the tsunamigenic potential associated with these events (e.g., Manzella et al., 2024). These processes, in fact, can involve mobilized volumes with different orders of magnitude higher (up to few of millions of cubic meters) than during normal volcanic activity, as evidenced by comparing the small-scale erosion observed outside the canyon area during the 2022–2023 (E3–5 in Fig. 5), that only accounts for ~130 × 10^3 m^3 (Table 2). This is in agreement with the common formation of local, small-scale landslide scars frequently observed over 20 years of bathymetric monitoring and associated with severe storm-waves affecting the NW flank of Stromboli during winter months (e.g., Casalbore et al., 2020; Di Traglia et al., 2022). To properly constrain the eroded volume from PDCs, this paper also indicates the need to perform topo-bathymetric surveys just after their occurrence, because of the rapid obliteration of related erosional features due to the emplacement of lava overflows in the aftermath of these catastrophic events (Calvari and Nunnari, 2023; Di Traglia et al., 2023b and 2024). This issue is witnessed by the observation of prevalent slope erosion, recorded by the survey realized just after the PDCs occurred between 9 and 15 October 2022 (Fig. 8a), with respect to the prevalent slope accretion observed within the canyon floor in the survey realized 12 days after the 4 December 2022 PDCs (Fig. 8c).

6. Conclusions

Stromboli volcano, because of its continuous eruptive activity, is one of the best cases to analyse the fast geomorphologic evolution in an active volcano, especially for the gradual and ongoing morphologic readjustment of the SdF slope that occurs here at high rates in response to different eruptive dynamics. Erosional and depositional processes have different times of occurrence and frequency, being active both in the *syn*-eruptive and post-eruptive stages and overall leading to consistent and rapid morphological variations, thus drastically reducing the preservation potential of related features.

In the case of the 2022 eruption, relevant erosive and depositional features developed on the subaerial and submarine SdF slope due to the 9 October 2022 and 4 December 2022 crater rim collapses and PDCs as well as to later reworking/gravity instability phenomena. Multitemporal topographic and bathymetric monitoring carried out over a 1-year time span (May 2022–May 2023) allowed the reconstruction of the main dynamics controlling the slope morphological evolution and related volumetric changes. These reconstructions are time-dependent, and thus the possibility to perform prompt surveys is mandatory for better constraining the scale and recurrence times of these phenomena, also in the view of geohazard assessment of potentially occurring future events.

Moreover, the reconstruction of events through the morphological monitoring shed light on the predisposing and controlling factors of the observed phenomena related to slope instability. In the case of SdF, besides first-order control from slope gradients, further constraints derive from the marked lithological/stratigraphic heterogeneity of the SdF filling, where different types of volcanic products are interlayered. Previous litho-morphological limits of lava flow fields formed in the last eruptions, in fact, influenced the location and limits of slope instability features, witnessing the role of inherited morphologies. A key role in the subaerial canyon formation, a feature that has never been described in the historical record of the SdF, is related to PDC's erosion that, in turn,

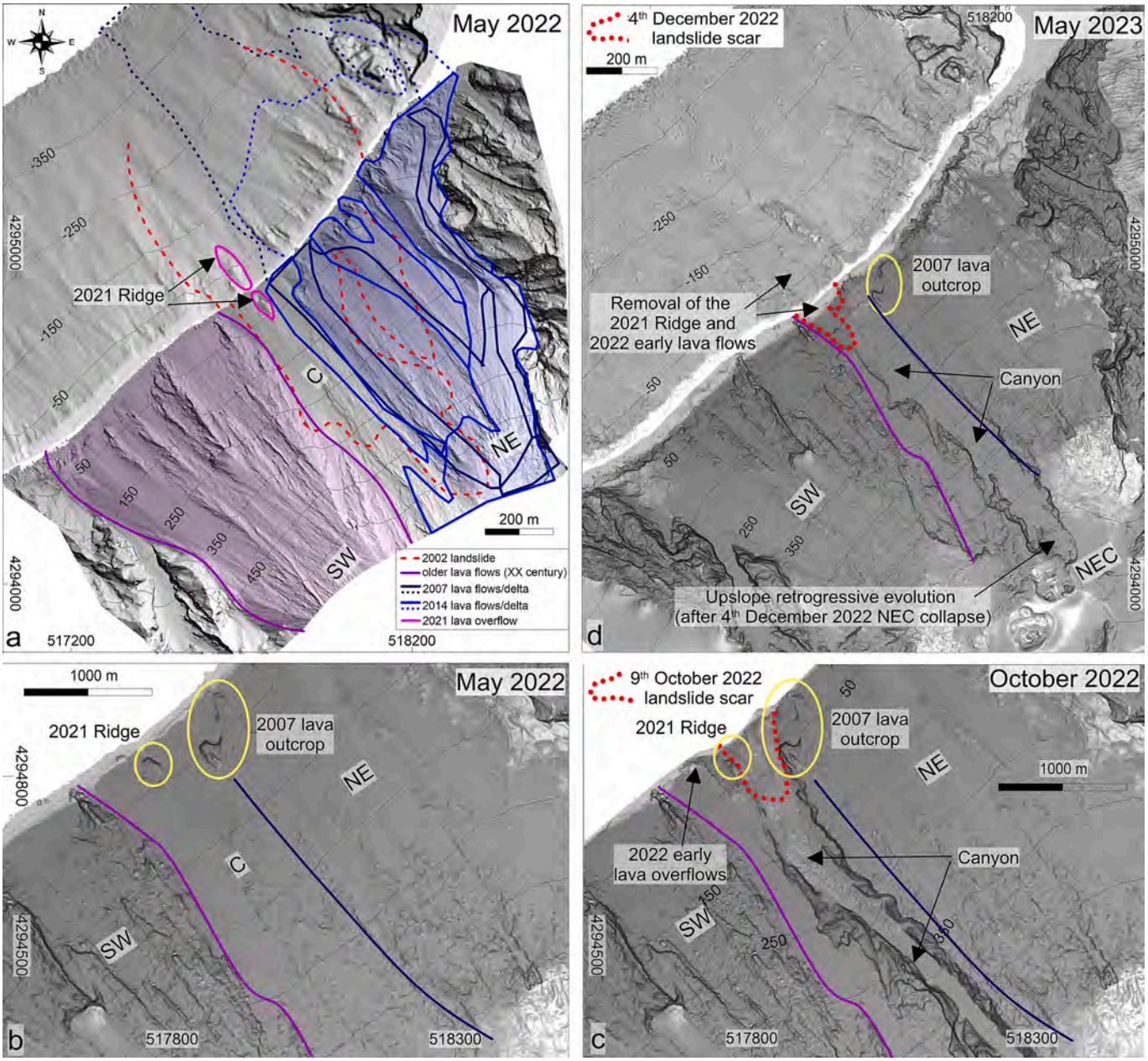

Fig. 14. a) May 2022 shaded relief map and isobath, with the indication of the 2002 tsunamigenic landslide scars as well as of the main lava flows limits along the NE, central and SW sectors of SdF. Note that the 2019 effusive event on the SW part is not significantly altered the morphology of this sector with respect to the older lava flows emplaced during the XX century. C: canyon. b) Zoom of the May 2022 shaded relief map (azimuthal illumination) in the NE sector of SdF, evidencing two remnants lava outcrops that have guided the location of the 9 October 2022 landslide scar and consequently that of the subaerial canyon in Fig. c). d) May 2023 shaded relief and isobath map, where a new coastal landslide (mapped with red dots) dismantled the SW limit of the 9 October 2022 slide, leading to the enlargement of the lowermost part of the canyon. Note that canyon enlargement also occurred along its flanks, especially the NE one, up to the limit of the 2007 lava flow field (blue line) extending down to the outcrop of remnant, massive lava.

triggered retrogressive slope instabilities starting from submarine and coastal sectors.

More generally, this study highlights how important is the integration of a land-to-sea monitoring system along the slope of active insular and coastal volcanoes for a better understanding of their overall morphological evolution in response to different volcanic dynamics, information that can be used to set-up a digital twin useful for basic and applied research, also considering the paucity of similar studies and available data in the literature.

CRediT authorship contribution statement

Daniele Casalbore: Investigation, Visualization, Writing – original draft, Conceptualization, Data curation. **Federico Di Traglia:** Resources, Visualization, Writing – original draft, Conceptualization. **Massimiliano Favalli:** Methodology, Data curation. **Alessandro Fornaciai:** Conceptualization, Visualization, Writing – original draft. **Claudia Romagnoli:** Conceptualization, Investigation, Writing – original draft. **Riccardo Civico:** Investigation, Writing – review & editing, Data curation. **Tullio Ricci:** Writing – review & editing, Data curation, Investigation. **Paolo Berardino:** Investigation. **Lorenzo Borselli:** Investigation. **Pierfrancesco Calabria:** Investigation. **Sonia Calvari:**

Data curation, Investigation, Resources, Writing – review & editing. **Tommaso Carlà:** Writing – review & editing. **Nicola Casagli:** Resources. **Francesco Casu:** Resources, Data curation, Investigation. **Francesco Latino Chiocci:** Resources, Visualization, Writing – review & editing. **Walter De Cesare:** Writing – review & editing. **Claudio De Luca:** Writing – review & editing. **Matteo Del Soldato:** Investigation. **Antonietta M. Esposito:** Writing – review & editing. **Carmen Esposito:** Investigation. **Flora Giudicepietro:** Resources, Writing – review & editing. **Teresa Gracchi:** Investigation, Data curation. **Riccardo Lanari:** Writing – review & editing, Data curation, Investigation, Resources. **Giovanni Macedonio:** Writing – review & editing. **Fernando Monterroso:** Investigation. **Antonio Natale:** Investigation, Data curation. **Teresa Nolesini:** Investigation, Writing – review & editing. **Stefano Perna:** Investigation, Data curation. **Denise Petronelli:** Data curation, Investigation. **Guglielmo Rossi:** Investigation. **Carlo Tacconi Stefanelli:** Investigation.

Declaration of competing interest

The authors declare that they have no known competing financial interests or personal relationships that could have appeared to influence the work reported in this paper.

Acknowledgements

We would like to express our gratitude to all the colleagues who have contributed to the monitoring efforts on Stromboli. Crew (Francesco Saggiomo and Marcello Felsani) of the small vessel used for bathymetric surveys is gratefully acknowledged along with Alessandro Rignani who performed the processing of multibeam data. Special thanks are also due to Sebastiano Cannavò (https://sebastianocannavostudio.com/) for providing us the images of the UAS survey performed on 9 October 2022.

The first author thanks also the funding provided by Progetto di Ateneo 2021 and 2022, University Sapienza of Rome, P.I. Daniele Casalbore as well as the RETURN (VS2) Extended Partnership. This research has benefited from the support from the following projects: "Convenzione B2 DPC-INGV 2022-2024, Stromboli"; INGV project Pianeta Dinamico 2023-2025 - ORME; INGV project Reti Multiparametriche (Task A2); INGV Progetto Strategico Dipartimentale 2019 "UNO"; INGV Progetto Strategico Dipartimentale 2019 "FIRST" (Delibera n. 144/2020); Accordo tra Università degli Studi di Firenze e Presidenza del Consiglio dei Ministri - Dipartimento della Protezione Civile 2022–2024; Accordo tra IREA-CNR e Presidenza del Consiglio dei Ministri - Dipartimento della Protezione Civile 2022–2024; Accordo tra IGAG-CNR e Presidenza del Consiglio dei Ministri - Dipartimento della Protezione Civile 2022–2024. The data used in this study were provided by INGV, UniFI, IGAG-CNR, UniRoma1 "La Sapienza", and IREA-CNR. We would like to acknowledge also the support of the Presidenza del Consiglio dei Ministri - Dipartimento della Protezione Civile. The contents of this paper represent the authors' ideas and do not necessarily correspond to the official opinion and policies of the Presidenza del Consiglio dei Ministri - Dipartimento della Protezione Civile. Partly funded by the European Union – Next Generation EU, National Recovery and Resilience Plan Mission 4 - Component 2. Project title: "Causes and consequences of deposit-derived pyroclastic density currents" (P20222BP7J).

We also acknowledge the support of EPOS-RI, including the one obtained through the EPOS-Italia JRU. The SSAP software research and development was funded by CONAHCYT (Mexico): Proyectos Ciencia Basica: CB-2016/286764. SSAP2010 is FREEWARE software, i.e. it is distributed free of charge only at HTTPS://WWW.SSAP.EU. There is only one full version of the SSAP2010 software and it is the free version that can be downloaded from the official website. The SSAP2010 User Licence allows the user unlimited use of the software with the ability to download all future updates from the web. SSAP20010 software is non-commercial software. Its distribution is non-profit (see SSAP User Licence).

We gratefully thank Tiago M. Alves, David Tappin and Morelia Urlaub, and Christopher Gomez for their useful comments that largely improved the quality of the manuscript.

Appendix A. Supplementary data

Supplementary data to this article can be found online at https://doi.org/10.1016/j.geomorph.2025.109961.

Data availability

The data presented in this study are available on request from the corresponding author. The data are not publicly available due to their acquisition for institutional purposes.

References

Barton, N., 2013. Shear strength criteria for rock, rock joints, rockfill and rock masses: problems and some solutions. J. Rock Mech. Geotech. Eng. 5 (4), 249–261.

Barton, N., Kjærnsli, B., 1981. Shear strength of rockfill. J. Geotech. Eng. Div. 107, 873–891.

Bedón, P.A.E., Ebmeier, S.K., Elliott, J.R., Wright, T.J., Mothes, P., Cayol, V., Maghsoudi, Y., Lazecký, M., Andrade, D., 2024. Co-eruptive, endogenous edifice growth, uplift during 4 years of eruption at Sangay Volcano, Ecuador. J. Volcanol. Geotherm. Res. 454, 108147.

Bernard, J., Kelfoun, K., Le Pennec, J.L., Vallejo Vargas, S., 2014. Pyroclastic flow erosion and bulking processes: comparing field-based vs. modeling results at Tungurahua volcano. Ecuador. Bulletin of Volcanology 76, 1–16.

Bonaccorso, A., Calvari, S., Garfì, G., Lodato, L., Patanè, D., 2003. Dynamics of the December 2002 flank failure and tsunami at Stromboli volcano inferred by volcanological and geophysical observations. Geophys. Res. Lett. 30 (18).

Borselli, L., 2020. SSAP 5.0 – Slope Stability Analysis Program. In: Manuale di riferimento del codice SSAP Versione 5.0. Researchgate. https://doi.org/10.13140/RG.2.2.12436.73604.

Borselli, L., 2023. SSAP 5.2- SLOPE STABILITY ANALYSIS PROGRAM″. User manual. https://doi.org/10.13140/RG.2.2.19931.03361.

Borselli, L., Capra, L., Sarocchi, D., De la Cruz-Reyna, S., 2011. Flank collapse scenarios at Volcán de Colima, Mexico: a relative instability analysis. J. Volcanol. Geotherm. Res. 208, 51–65.

Bosman, A., Casalbore, D., Romagnoli, C., Chiocci, F.L., 2014. Formation of an 'a'ā lava delta: insights from time-lapse multibeam bathymetry and direct observations during the Stromboli 2007 eruption. Bull. Volcanol. 76, 1–12.

Brand, B.D., Mackaman-Lofland, C., Pollock, N.M., Bendaña, S., Dawson, B., Wichgers, P., 2014. Dynamics of pyroclastic density currents: conditions that promote substrate erosion and self-channelization—Mount St Helens, Washington (USA). J. Volcanol. Geotherm. Res. 276, 189–214.

Brand, B.D., Bendaña, S., Self, S., Pollock, N., 2016. Topographic controls on pyroclastic density current dynamics: insight from 18 May 1980 deposits at Mount St. Helens, Washington (USA). J. Volcanol. Geotherm. Res. 321, 1–17.

Calder, E.S., Sparks, R.S.J., Gardeweg, M.C., 2000. Erosion, transport and segregation of pumice and lithic clasts in pyroclastic flows inferred from ignimbrite at Lascar Volcano, Chile. J. Volcanol. Geotherm. Res. 104 (1–4), 201–235.

Calvari, S., Nunnari, G., 2023. Statistical insights on the eruptive activity at Stromboli Volcano (Italy) recorded from 1879 to 2023. Remote Sens. 15 (19), 4822.

Calvari, S., Spampinato, L., Lodato, L., Harris, A.J., Patrick, M.R., Dehn, J., Andronico, D., 2005. Chronology and complex volcanic processes during the 2002–2003 flank eruption at Stromboli volcano (Italy) reconstructed from direct observations and surveys with a handheld thermal camera. J. Geophys. Res. Solid Earth 110 (B2).

Calvari, S., Lodato, L., Steffke, A., Cristaldi, A., Harris, A.J.L., Spampinato, L., Boschi, E., 2010. The 2007 Stromboli eruption: event chronology and effusion rates using thermal infrared data. J. Geophys. Res. Solid Earth 115 (B4).

Calvari, S., Di Traglia, F., Ganci, G., Bruno, V., Ciancitto, F., Di Lieto, B., Belviso, P., 2022. Multi-parametric study of an eruptive phase comprising unrest, major explosions, crater failure, pyroclastic density currents and lava flows: Stromboli volcano, 1 December 2020–30 June 2021. Front. Earth Sci. 10, 899635.

Casalbore, D., Romagnoli, C., Chiocci, F., Frezza, V., 2010. Morpho-sedimentary characteristics of the volcaniclastic apron around Stromboli volcano (Italy). Mar. Geol. 269 (3–4), 132–148.

Casalbore, D., Passeri, F., Tommasi, P., Verrucci, L., Bosman, A., Romagnoli, C., Chiocci, F.L., 2020. Small-scale slope instability on the submarine flanks of insular volcanoes: the case-study of the Sciara del Fuoco slope (Stromboli). Int. J. Earth Sci. 109, 2643–2658.

Casalbore, D., Di Traglia, F., Bosman, A., Romagnoli, C., Casagli, N., Chiocci, F.L., 2021. Submarine and subaerial morphological changes associated with the 2014 eruption at Stromboli Island. Remote Sens 13 (11), 2043.

Casalbore, D., Di Traglia, F., Romagnoli, C., Favalli, M., Gracchi, T., Tacconi Stefanelli, C., Chiocci, F.L., 2022. Integration of remote sensing and offshore

geophysical data for monitoring the short-term morphological evolution of an active volcanic flank: a case study from Stromboli Island. Remote Sens 14 (18), 4605.
Chiocci, F.L., Romagnoli, C., Tommasi, P., Bosman, A., 2008a. The Stromboli 2002 tsunamigenic submarine slide: characteristics and possible failure mechanisms. J. Geophys. Res. Solid Earth 113 (B10).
Chiocci, F.L., Romagnoli, C., Bosman, A., 2008b. Morphologic resilience and depositional processes due to the rapid evolution of the submerged Sciara del Fuoco (Stromboli Island) after the December 2002 submarine slide and tsunami. Geomorphology 100 (3–4), 356–365.
Civico, R., Ricci, T., Scarlato, P., Andronico, D., Cantarero, M., Carr, B.B., Taddeucci, J., 2021. Unoccupied aircraft systems (UASs) reveal the morphological changes at Stromboli Volcano (Italy) before, between, and after the 3 July and 28 August 2019 Paroxysmal Eruptions. Remote Sens 13 (15), 2870.
Civico, R., Ricci, T., Cecili, A., Scarlato, P., 2024. High-resolution topography reveals morphological changes of Stromboli volcano following the July 2024 eruption. Sci. Data 11 (1), 1219.
Clare, M.A., Yeo, I.A., Watson, S., Wysoczanski, R., Seabrook, S., Mackay, K., Williams, M., 2023. Fast and destructive density currents created by ocean-entering volcanic eruptions. Science 381 (6662), 1085–1092.
Cole, P.D., Fernandez, E., Duarte, E., Duncan, A.M., 2005. Explosive activity and generation mechanisms of pyroclastic flows at Arenal volcano, Costa Rica between 1987 and 2001. Bull. Volcanol. 67, 695–716.
de Dolomieu, D., 1783. Viaggio alle Isole Lipari. Eds. Magenes, 2022 (in Italian; Translated into Italian from French).
Di Traglia, F., Calvari, S., D'Auria, L., Nolesini, T., Bonaccorso, A., Fornaciai, A., Casagli, N., 2018a. The 2014 effusive eruption at Stromboli: New insights from in situ and remote-sensing measurements. Remote Sens 10 (12), 2035.
Di Traglia, F., Nolesini, T., Ciampalini, A., Solari, L., Frodella, W., Bellotti, F., Casagli, N., 2018b. Tracking morphological changes and slope instability using spaceborne and ground-based SAR data. Geomorphology 300, 95–112.
Di Traglia, F., Nolesini, T., Solari, L., Ciampalini, A., Frodella, W., Steri, D., Casagli, N., 2018c. Lava delta deformation as a proxy for submarine slope instability. Earth Planet. Sci. Lett. 488, 46–58.
Di Traglia, F., Fornaciai, A., Favalli, M., Nolesini, T., Casagli, N., 2020. Catching geomorphological response to volcanic activity on steep slope volcanoes using multi-platform remote sensing. Remote Sens 12 (3), 438.
Di Traglia, F., De Luca, C., Manzo, M., Nolesini, T., Casagli, N., Lanari, R., Casu, F., 2021. Joint exploitation of space-borne and ground-based multitemporal InSAR measurements for volcano monitoring: the Stromboli volcano case study. Remote Sens. Environ. 260, 112441.
Di Traglia, F., Fornaciai, A., Casalbore, D., Favalli, M., Manzella, I., Romagnoli, C., Casagli, N., 2022. Subaerial-submarine morphological changes at Stromboli volcano (Italy) induced by the 2019–2020 eruptive activity. Geomorphology 400, 108093.
Di Traglia, F., Calvari, S., Borselli, L., Cassanego, L., Giudicepietro, F., Macedonio, G., Casagli, N., 2023a. Assessing flank instability of Stromboli volcano (Italy) by reappraising the 30 December 2002 tsunamigenic landslides. Landslides 20 (7), 1363–1380.
Di Traglia, F., Borselli, L., Nolesini, T., Casagli, N., 2023b. Crater-rim collapse at Stromboli volcano: understanding the mechanisms leading from the failure of hot rocks to the development of glowing avalanches. Nat. Hazards 115 (3), 2051–2068.
Di Traglia, F., Berardino, P., Borselli, L., Calabria, P., Calvari, S., Casalbore, D., Stefanelli, C.T., 2024. Generation of deposit-derived pyroclastic density currents by repeated crater rim failures at Stromboli Volcano (Italy). Bull. Volcanol. 86 (8), 69.
Ebmeier, S.K., Biggs, J., Muller, C., Avard, G., 2014. Thin-skinned mass-wasting responsible for widespread deformation at Arenal volcano. Front. Earth Sci. 2, 35.
Esposito, A.M., D'Auria, L., Giudicepietro, F., Peluso, R., Martini, M., 2012. Automatic recognition of landslide seismic signals based on neural network analysis of seismic signals: an application to the monitoring of Stromboli volcano (Southern Italy). Pure Appl. Geophys. 170, 1821–1832.
Esposito, C., Berardino, P., Natale, A., Lanari, R., Perna, S., 2023. Stromboli volcano topography variations retrieval through airborne single-pass SAR interferometry. In: IGARSS 2023–2023 IEEE International Geoscience and Remote Sensing Symposium. IEEE, pp. 7989–7992.
Esposito, C., Natale, A., Lanari, R., Berardino, P., Perna, S., 2024. On the capabilities of the IREA-CNR airborne SAR infrastructure. Remote Sens 16 (19), 3704.
Falsaperla, S., Maiolino, V., Spampinato, S., Jaquet, O., Neri, M., 2008. Sliding episodes during the 2002–2003 Stromboli lava effusion: insights from seismic, volcanic, and statistical data analysis. Geochem. Geophys. Geosyst. 9, Q04022.
Favalli, M., Fornaciai, A., Mazzarini, F., Harris, A., Neri, M., Behncke, B., Pareschi, M.T., Tarquini, S., Boschi, E., 2010. Evolution of an active lava flow field using a multitemporal LIDAR acquisition. J. Geophys. Res. Solid Earth 115 (B11).
Favalli, M., Fornaciai, A., Nannipieri, L., Harris, A., Calvari, S., Lormand, C., 2018. UAV-based remote sensing surveys of lava flow fields: a case study from Etna's 1974 channel-fed lava flows. Bull. Volcanol. 80, 1–18.
Fornaciai, A., Favalli, M., Nannipieri, L., 2019. Numerical simulation of the tsunamis generated by the Sciara del Fuoco landslides (Stromboli Island, Italy). Sci. Rep. 9 (1), 18542.
Francalanci, L., Lucchi, F., Keller, J., De Astis, G., Tranne, C.A., 2013. Chapter 13 Eruptive, volcano-tectonic and magmatic history of the Stromboli volcano (north-eastern Aeolian archipelago). Geol. Soc. Lond. Mem. 37 (1), 397–471.
Franceschetti, G., Lanari, R., 1999. Synthetic Aperture Radar Processing. CRC PRESS, New York.
Freundt, A., 2003. Entrance of hot pyroclastic flows into the sea: experimental observations. Bull. Volcanol. 65 (2), 144–164.
Gallant, E., Deng, F., Connor, C.B., Dixon, T.H., Xie, S., Saballos, J.A., Thompson, G., 2020. Deep and rapid thermo-mechanical erosion by a small-volume lava flow. Earth Planet. Sci. Lett. 537, 116163.
Giudicepietro, F., López, C., Macedonio, G., Alparone, S., Bianco, F., Calvari, S., De Cesare, W., Delle Donne, D., Di Lieto, B., Esposito, A.M., Orazi, M., 2020. Geophysical precursors of the July-August 2019 paroxysmal eruptive phase and their implications for Stromboli volcano (Italy) monitoring. Sci. Rep. 10 (1), 10296.
Giudicepietro, F., Calvari, S., De Cesare, W., Di Lieto, B., Di Traglia, F., Esposito, A.M., Macedonio, G., 2023. Seismic and thermal precursors of crater collapses and overflows at Stromboli volcano. Sci. Rep. 13 (1), 11115.
Gracchi, T., Tacconi Stefanelli, C., Rossi, G., Di Traglia, F., Nolesini, T., Tanteri, L., Casagli, N., 2022. UAV-based multitemporal remote sensing surveys of volcano unstable flanks: a case study from stromboli. Remote Sens 14 (10), 2489.
Haep, M.J., Villeneuve, M., Albino, F., et al., 2020. Towards more realistic values of elastic moduli for volcano modelling. J. Volcanol. Geotherm. Res. 390, 106684.
Hoek, E., Brown, E.T., 2019. The Hoek-Brown failure criterion and GSI–2018 edition. J. Rock Mech. Geotech. Eng. 11 (3), 445–463.
Hoek, E., Carranza-Torres, C.T., Corkum, B., 2002. Hoek–Brown failure criterion—2002 edition. In: Proc. North American Rock Mechanics Society-TAC Conference, Toronto, July 2002, 1, pp. 267–273.
Kokelaar, P., Romagnoli, C., 1995. Sector collapse, sedimentation and clast population evolution at an active island-arc volcano: Stromboli, Italy. Bull. Volcanol. 57, 240–262.
Lube, G., Cronin, S.J., Platz, T., Freundt, A., Procter, J.N., Henderson, C., Sheridan, M.F., 2007. Flow and deposition of pyroclastic granular flows: a type example from the 1975 Ngauruhoe eruption, New Zealand. J. Volcanol. Geotherm. Res. 161 (3), 165–186.
Lunardi, P., Froldi, P., Fornari, E., 1994. Rock mechanics investigations for rock slope stability assessment. Int. J. Rock Mech. Min. Sci. Geomech. Abstr. 31 (4), 323–345. Pergamon.
Manzella, I., Makris, S., Casalbore, D., Cole, P., Kelfoun, K., Georgiopoulou, A., van Westen, C., 2024. Cascading hazards in volcanic environments: monitoring, modelling and impact analysis of tsunamigenic flows for risk reduction. Ann. Geophys. 67 (4).
Maramai, A., Graziani, L., Tinti, S., 2005. Tsunamis in the Aeolian Islands (southern Italy): a review. Mar. Geol. 215 (1–2), 11–21.
Marsella, M., Baldi, P., Coltelli, M., Fabris, M., 2012. The morphological evolution of the Sciara del Fuoco since 1868: reconstructing the effusive activity at Stromboli volcano. Bull. Volcanol. 74, 231–248.
Mercalli, G., 1883. Vulcani e fenomeni vulcanici in Italia, 3. A. Forni.
Natale, A., Berardino, P., Esposito, C., Palmese, G., Lanari, R., Perna, S., 2022, July. The New Italian airborne multiband interferometric and polarimetric SAR (MIPS) system: first flight test results. In: IGARSS 2022–2022 IEEE International Geoscience and Remote Sensing Symposium. IEEE, pp. 4506–4509.
Pistolesi, M., Bertagnini, A., Di Roberto, A., Ripepe, M., Rosi, M., 2020. Tsunami and tephra deposits record interactions between past eruptive activity and landslides at Stromboli volcano, Italy. Geology 48 (5), 436–440.
Re, G., Pompilio, M., Del Carlo, P., Di Roberto, A., 2022. Physical and morphological characterization of the 19 May 2021 ash cloud deposit at Stromboli (Italy). Sci. Rep. 12, 10777.
Ripepe, M., Lacanna, G., 2024. Volcano generated tsunami recorded in the near source. Nat. Commun. 15 (1), 1802.
Romagnoli, C., Casalbore, D., Chiocci, F.L., Bosman, A., 2009a. Offshore evidence of large-scale lateral collapses on the eastern flank of Stromboli, Italy, due to structurally-controlled, bilateral flank instability. Mar. Geol. 262 (1–4), 1–13.
Romagnoli, C., Kokelaar, P., Casalbore, D., Chiocci, F.L., 2009b. Lateral collapses and active sedimentary processes on the northwestern flank of Stromboli volcano, Italy. Mar. Geol. 265 (3–4), 101–119.
Rosen, P.A., Hensley, S., Joughin, I.R., Li, F.K., Madsen, S.N., Rodríguez, E., Goldstein, R. M., 2000. Synthetic aperture radar interferometry. Proc IEEE 8 (3), 333–382.
Rosi, M., Levi, S.T., Pistolesi, M., Bertagnini, A., Brunelli, D., Cannavò, V., Yoon, D., 2019. Geoarchaeological evidence of middle-age tsunamis at Stromboli and consequences for the tsunami hazard in the Southern Tyrrhenian Sea. Sci. Rep. 9 (1), 677.
Sarocchi, D., Sulpizio, R., Macías, J.L., Saucedo, R., 2011. The 17 July 1999 block-and-ash flow (BAF) at Colima Volcano: new insights on volcanic granular flows from textural analysis. J. Volcanol. Geotherm. Res. 204 (1–4), 40–56.
Smellie, J.L., Wilch, T.I., Rocchi, S., 2013. 'A 'ā lava-fed deltas: a new reference tool in paleoenvironmental studies. Geology 41 (4), 403–406.
Stevenson, J.A., Mitchell, N.C., Mochrie, F., Cassidy, M., Pinkerton, H., 2012. Lava penetrating water: the different behaviours of pāhoehoe and 'a 'ā at the Nesjahraun, Þingvellir, Iceland. Bull. Volcanol. 74, 33–46.
Thouret, J.C., 1999. Volcanic geomorphology—an overview. Earth Sci. Rev. 47 (1–2), 95–131.
Tinti, S., Manucci, A., Pagnoni, G., Armigliato, A., Zaniboni, F., 2005. The 30 December 2002 landslide-induced tsunamis in Stromboli: sequence of the events reconstructed from the eyewitness accounts. Nat. Hazards Earth Syst. Sci. 5 (6), 763–775.
Tioukov, V., Giudicepietro, F., Macedonio, G., Calvari, S., Di Traglia, F., Fornaciai, A., Favalli, M., 2022. Structure of the shallow supply system at Stromboli Volcano, Italy, through integration of muography, digital elevation models, seismicity, and ground deformation data. In: Muography Exploring Earth's Subsurface with Elementary Particles, pp. 75–91.
Trofimovs, J., Amy, L., Boudon, G., et al., 2006. Submarine pyroclastic deposits formed at the Soufrière Hills volcano, Montserrat (1995–2003): what happens when pyroclastic flows enter the ocean? Geology 34 (7), 549–552.

Tucker, D.S., Scott, K.M., 2009. Structures and facies associated with the flow of subaerial basaltic lava into a deep freshwater lake: the Sulphur Creek lava flow, North Cascades, Washington. J. Volcanol. Geotherm. Res. 185 (4), 311–322.

Verrucci, L., Tommasi, P., Boldini, D., Graziani, A., Rotonda, T., 2019. Modelling the instability phenomena on the NW flank of Stromboli Volcano (Italy) due to lateral dyke intrusion. J. Volcanol. Geotherm. Res. 371, 245–262.

Williams, R., 2012. DEMs of difference. Geomorphol. Tech. 2 (3.2).